

Qualification of Temperature Sensors  
for the Pacific Ocean Neutrino Experiment  
for long-term Temperature Monitoring

---

Martin Dinkel

May 12, 2022

Bachelor Thesis



Chair of Experimental Physics with Cosmic Particles

**Supervisor:** Prof. Dr. Elisa Resconi  
**Advisor:** M.Sc. Christian Spannfellner



## Acknowledgments

First I like to thank my supervising professor Elisa Resconi for providing this interesting topic for my bachelor thesis. Furthermore, I want to thank her for giving me the opportunity to give a talk at the Deutsche Physiker Gesellschaft conference 2022 about P-ONE-1.

Evenly, I want to express my gratitude to my advisor M.Sc. Christian Spannfellner for all the help at any time over the whole period of my bachelor thesis. Thanks for all the introductions in the different software applications, auxiliary explanations and fruitful discussions.

Finally, I want to thank all my family and friends for their support, endurance and distraction during the whole period. Thank you!

## Abstract

The Pacific Ocean Neutrino Experiment (P-ONE) is a large scale neutrino telescope currently under development, which will be located in the deep sea at Cascadia Basin in the North-East Pacific 200 km offshore Vancouver. At the moment the development of the first prototype line P-ONE-1 of the P-ONE detector is at work. As the P-ONE telescope aims for an operating time of over 15 years the housings of the modules for detection of Cherenkov light and calibration at the mooring lines can be used for hosting environmental sensors to monitor long-term the ambiance parameters of the deep sea. In face of that this bachelor thesis is about the research and development of temperature sensors for this application.

After an introduction to astroparticle physics and neutrino detection, this thesis will present the current development status of the prototype line P-ONE-1 of the P-ONE telescope. Then the Pathfinder missions at Cascadia Basin and their results concerning the background measurement of bioluminescence are envisioned as well as possible measurement of deep ocean parameters in correlation to bioluminescence measurements. Based on that the research and selection of possible temperature sensors to monitor the deep sea temperature is presented. Three temperature sensors have been selected to be tested: TMP 117 digital temperature sensor, Pt100 analog temperature sensor and the industrial calibrated Starmon Mini temperature recorder as reference. For the TMP 117 and the Pt100 sensor the development of the readout electronics is displayed. Subsequent the different testing measurement of the temperature sensors are explicated and the results evaluated. The TMP 117 seems to be a promising candidate for usage as a temperature sensor to monitor long-term the deep sea temperature, whereas the Pt100 sensor showed a non-constant offset and a strong noise, wherefore an accurate temperature measurement with this sensor was not feasible. Finally a prospect to the following proceeding is given wherein more detailed measurements for the better characterization of the TMP 117 are recommended and the development of a housing for the temperature sensor is suggested.

# Contents

<b>1</b>	<b>Astroparticle Physics Introduction</b>	<b>1</b>
<b>2</b>	<b>Theoretical Background of Cosmic Neutrinos</b>	<b>3</b>
2.1	Sources of High Energy Cosmic Neutrinos . . . . .	3
2.2	Interaction of Cosmic Neutrinos with Matter . . . . .	4
2.3	Detection Principles of Cosmic Neutrinos . . . . .	6
<b>3</b>	<b>The Pacific Ocean Neutrino Experiment</b>	<b>8</b>
3.1	P-ONE-1 . . . . .	9
3.1.1	P-ONE Optical Module . . . . .	10
3.1.2	P-ONE Calibration Module . . . . .	11
3.2	Pathfinder Missions in Cascadia Basin . . . . .	12
3.2.1	Overview about the Pathfinder Missions . . . . .	12
3.2.2	Background Measurement of Bioluminescence . . . . .	15
3.3	Possible Measurements of Deep Ocean Parameters in Correlation to Bioluminescence Measurements . . . . .	15
<b>4</b>	<b>Development of Deep Ocean Temperature Measurement Facilities for P-ONE</b>	<b>16</b>
4.1	Research and Selection for Possible Temperature Sensors . . . . .	16
4.1.1	Starmon Mini Temperature Recorder . . . . .	18
4.1.2	TMP 117 Digital Temperature Sensor . . . . .	18
4.1.3	P0K1.232.4W.K.010 Platinum Sensor with Wires . . . . .	19
4.2	Development of Readout Electronics for the Temperature Sensors . . . . .	20
4.2.1	Readout Electronics of the TMP117 . . . . .	20
4.2.2	Readout Electronics of P0K1.232.4W.K.010 Platinum Pt100 Sensor . . . . .	20
4.3	Experimental Setup for Testing the Temperature Sensors . . . . .	23
4.4	Test Procedures and Data Measurements . . . . .	24
4.4.1	Measurement for the General Characterization of the Different Temperature Sensors . . . . .	24
4.4.2	Measurement for Detailed Characterization of the Different Temperature Sensors . . . . .	27
4.4.3	Measurement of the Response Time of the Temperature Sensors . . . . .	29
4.4.4	Measurement of four TMP 117 Digital Temperature Sensors of Different Production Lines . . . . .	31
4.4.5	Stress Test Measurements of the TMP 117 Digital Temperature Sensor . . . . .	36
4.5	Evaluation of the Measurement Results . . . . .	38
4.6	Prospect to Following Proceeding . . . . .	39
<b>A</b>	<b>Appendix</b>	<b>40</b>
A.1	TMP 117 Digital Temperature Sensor . . . . .	40
A.2	P0K1.232.4W.K.010 Platinum Sensor with Wires . . . . .	42
A.3	Temperature Chamber Programs . . . . .	44

A.4 Arduino Programs . . . . .	48
--------------------------------	----



# 1 Astroparticle Physics Introduction

This bachelor thesis is about the development of temperature sensors for the Pacific Ocean Neutrino Experiment (P-ONE) for long-term temperature monitoring and correlation study of bioluminescence events. The P-ONE is a neutrino telescope currently under development which will be located in the deep sea in the North-East Pacific. For understanding the working principle of the neutrino telescope first a introduction in the astroparticle physics is made, then the P-ONE telescope will be introduced and finally the development of the temperature sensors for the P-ONE will be presented.

The detection and study of cosmic messengers are fundamental for the knowledge of acceleration and production mechanisms of the astrophysical sources [1]. By just observing cosmic rays it is difficult to identify sources of ultra high energy cosmic rays due to magnetic fields that deflect the cosmic rays inside and outside the Galaxy. Different messengers such as cosmic-rays, gamma-rays, gravitational waves and neutrinos can provide complementary information. The Multimessenger Astronomy is combining the information of cosmic rays with information provided by the other cosmic messengers. [2]

The different cosmic messengers will be introduced in the following.

## Cosmic-Rays

Cosmic rays are mainly ionized nuclei composed of high energy protons, alpha particles and heavier nuclei. Cosmic rays outside the atmosphere are called primary cosmic rays. While travelling towards Earth's surface, these particles interact with the atmospheric nuclei causing an air shower of new particles called secondary cosmic rays. [1, 3] The reaction of a cosmic ray proton with a nuclei from the atmosphere is shown in formula 1.1 [4]:

$$p + N \rightarrow \pi^{\pm}, \pi^0, K^{\pm}, K^0, p, n, \dots \quad (1.1)$$

Hereby the secondary cosmic rays can decay hadronic, wherein mainly neutrons, protons, kaons, pions are created which interact strongly with nuclei in the air causing a cascade of hadronic particles with variable energies, so called hadronic showers [3]. An electromagnetic component is added via the decay of pions and the subsequent production of positrons and electrons. The decay of the neutral pions plays hereby a relevant role.

$$\pi^0 \rightarrow \gamma + \gamma \quad (1.2)$$

Additionaly photons can be generated by bremsstrahlung of charged particles. [3]

## Gamma-Rays

Gamma rays are produced by cosmic rays along their path when propagating through the universe by various processes. One of these processes is caused by magnetic fields which leads

to the emissions of gamma-rays via synchrotron radiation, another one is bremsstrahlung caused by electric fields. Also the decay of a neutral pion which was created by a collision of cosmic rays with gas molecules contribute to the production. As shown in 1.2 the neutral pion decays subsequently into two gammas. A further process is the inverse Compton effect, wherein ultra-relativistic electrons or other charged particles scatter on photons and transfer some of their energy to the photon resulting in a high energy gamma-ray. [3, 4]

In relation to the detection of gamma rays, it has to be considered that the universe, and also the atmosphere, is opaque to photons with certain wavelength and thus acts like a filter. There are two different main detection techniques established. The first is space-based and covers a broad energy region from a few MeV to a few GeV. The second is ground-based and is based on detecting Cherenkov radiation emitted by secondary particles produced by the interaction of gamma rays with nuclei of the atmosphere. The Cherenkov radiation is also important for the field of research of neutrino astronomy and will be further highlighted in section 2.3. [3, 4]

### Gravitational Waves

Gravitational waves are tiny distortions of space-time generated by accelerated or deformed huge masses. They can propagate from their source with the speed of light and are caused by the most violent and highly energetic events in the universe, e.g. the collapse of two black holes, the merging of two neutron stars, or supernovae. By propagating from their source through the universe they disrupt space-time by squeezing and dragging. The first physically measured distortion of space-time, caused by two colliding black holes, could be measured at September 14th, 2015 by the two Laser Interferometer Gravitational-Wave Observatory (LIGO) interferometers. [1, 3, 5]

### Neutrinos

Neutrinos are solely weakly interacting particles. Therefore they have no electric charge and a low cross section for which reason they are not deflected by magnetic fields along their path from their source to the Earth. Corresponding to the standard model of particle physics they are leptons and have three flavors corresponding to the charged leptons electron, muon and tau. Additionally they have a small mass below  $m_\nu < 0.8 \text{ eV}$ . [1, 6]

Due to the existence of a mass of the neutrino the transition between different neutrino flavors is possible: the flavor lepton numbers  $L_e, L_\mu, L_\tau$  are not conserved. This also implies that the neutrino's flavor eigenstates  $|\nu_\alpha\rangle$  and the mass eigenstates  $|\nu_i\rangle$  are different. The relationship between flavor and mass eigenstates can be written as

$$|\nu_\alpha\rangle = \sum_i U_{\alpha i} |\nu_i\rangle, \quad (1.3)$$

wherein  $\alpha = e, \mu, \tau$ ,  $i = 1, 2, 3$  and  $U_{\alpha i}$  is the 3x3 Pontecorvo-Maki-Nakagawa-Sakata (PMNS) mixing matrix, which connects the flavor and mass eigenstates. Hence a flavor eigenstate is a quantum mechanic superposition of the three mass eigenstates. As the different mass eigenstates

propagate at different speeds through space, the quantum mechanical superposition changes by the distance to the source and thus the probability of detecting a determined flavor eigenstate changes with distance. From this it follows that a neutrino which was produced in certain flavor eigenstate can be detected with a different flavor caused by the so called neutrino-oscillation. [3, 5]

## 2 Theoretical Background of Cosmic Neutrinos

The focus of this thesis lies especially on high-energy cosmic neutrinos which originate within the galaxy or are of extra galactic origin. The advantage in relation to other cosmic messengers is that neutrinos are not deflected by magnetic or electric fields while propagating through space. Therefore the detection of cosmic neutrinos allows point source searches. Also, cosmic rays are limited to a horizon of around 100 Mpc at an energy of  $10^{20}$  eV because of the interaction with photons of the Cosmic Microwave Background (CMB) at higher energies. The gamma horizon is limited by interactions of gammas with the infrared and CMB. On the other hand, as neutrinos only interact weakly and have a small mass is a disadvantage, because the detection of neutrinos poses to be very difficult due to the small interaction chance. [3, 5]

### 2.1 Sources of High Energy Cosmic Neutrinos

Astrophysical high-energy neutrinos are produced by the decay of charged pions. Pions can be created by accelerated protons through hadronuclear interactions, or through photoproduction from cosmic-ray protons interacting with ambient photons. In beam dump processes mesons are produced by the collision of two protons:

$$p + p \rightarrow \pi^{\pm}, \pi^0, K^{\pm}, K^0, p, n \quad (2.1)$$

By this collision process almost the same number of  $\pi^0, \pi^+, \pi^-$  are produced, wherein for the production of high-energy neutrinos the decay of the charged pions are of note as they decay as:

$$\pi^- \rightarrow \mu^- \bar{\nu}_{\mu}; \quad \mu^- \rightarrow e^- \bar{\nu}_e \nu_{\mu} \quad (2.2)$$

For the  $\pi^+$  the process is the charge-conjugate reaction. Thus, for one charged pion there are three neutrinos produced. Another process to produce secondary mesons is the photoproduction process where high-energy protons interact with low-energy photons in the surroundings of their sources:

$$p + \gamma \rightarrow \Delta^+ \rightarrow \pi^0 + p \rightarrow \pi^+ + n \quad (2.3)$$

The decay of the secondary charged pions of this process is the same as in formula 2.2 shown. To generate high-energy cosmic-rays, which are the primary source of high-energy cosmic neutrinos,

there are particle acceleration mechanisms necessary. Cosmic accelerators are known within our galaxy and beyond, wherein there are still open questions regarding the origin of high-energy cosmic rays. [3, 4]

### Galactic Accelerators

One kind of galactic accelerators are Supernova Remnants (SNRs). SNRs are the result of supernovae, wherein the stellar core will be compressed due to the gravitational pressure and a rise in the electron Fermi energy allows the generation of neutrons and neutrinos via

$$e^{-} + p \rightarrow n + \nu_e . \quad (2.4)$$

As neutrinos are solely weakly interacting they can escape the concentrated matter. Next to this emission of neutrinos, also a emission of high-energy cosmic rays is caused by the degeneration of the core and consequential the shock wave, which creates the explosion. [5]

Pulsar Wind Nebulae (PWN) are SNRs powered by a pulsar in their center. Pulsars are rapidly rotating neutron stars, which have a extremely high magnetic field, through that charged particles can be magnetically accelerated. Another possible accelerator candidate are binary systems, wherein a compact object, as for example a neutron star or a black hole, is increasing its mass by accretion of matter from a donor companion and thereby gravitational potential energy is released. Caused by the massive flow of ionized matter large electromagnetic fields are created, which produce the energy to accelerate cosmic particles to high energies. [4, 5]

### Extragalactic Accelerators

Based on the current knowledge about acceleration mechanisms, there are no known galactic sources which can provide the so-called Ultra High Energy Cosmic Rays (UHECR) . These UHECRs reach an energy beyond  $10^{19}$  eV. Extragalactic sources are considered to be able to achieve such acceleration energies. The first possible candidate is the most luminous sources in universe, the Active Galactic Nuclei (AGN). A supermassive blackhole accretes matter and adjacent emits two relativistic particle jets perpendicular to the accretion disk. These jets are able of accelerating particles to high and probably ultra-high energies. If the jet cone of an AGN points towards the Earth it is called blazar [3, 4]. A second candidate are Gamma Ray Bursts (GRBs), wherein their origin is not yet fully understood. It is supposed that there must be a powerful driving force behind this phenomenon, for instance hypernovae, the merger of two neutron stars or a neutron star with a black hole. [3, 5, 7]

## 2.2 Interaction of Cosmic Neutrinos with Matter

As already mentioned in chapter 1, neutrinos are solely interacting weakly with other particles. Generally there are two different types of interactions of neutrinos with matter which are shown in figure 2.1. There is the neutral current (NC) interaction and the charged current (CC) interaction.

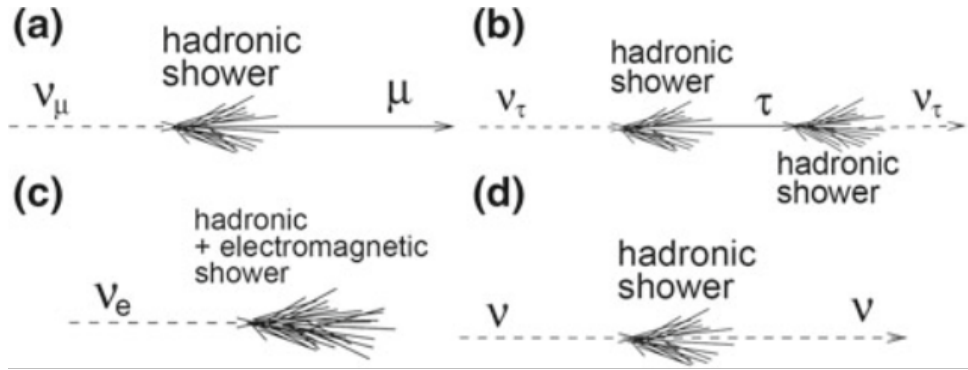


Fig. 2.1: Signature topology for neutrino interaction types with matter. (a), (b) and (c) show the flavor dependent charged current interaction types, and (d) the flavor independent neutral current interaction process.[4]

The first type of interaction of neutrinos with matter is as already mentioned above the CC interaction. Hereby the flavor of the neutrino is relevant for the interaction mechanism.

As shown in figure 2.1 (a) a muon neutrino  $\nu_\mu$  produces at the CC interaction with matter a hadronic shower, like at the NC interaction. In contrast to the neutral current interaction, at the CC interaction of a muon neutrino a secondary muon is created. While the secondary muon propagates through the matter, it creates a track like signature, wherein photons, produced by the secondary muon propagating, are scattered and absorbed by the medium. These photons are produced by the Cherenkov effect, which be explained in more detail in section 2.3.

The CC interaction of a tau neutrino  $\nu_\tau$  with matter is demonstrated in figure 2.1 schema (b). This process contains two hadronic shower events. The first is created at the first vertex, when the tau neutrino interacts with a nucleus of matter, wherein a secondary tau is produced. The secondary tau propagates through the matter and decays into a tau neutrino by producing a hadronic shower. The distance the secondary tau can travel depends on the energy of the tau. If the tau has enough energy and therefore can travel a distance which allows a separated detection of the first and the second hadronic shower, the signature of the charged current interaction of the tau neutrino is called double bang event.

The electron neutrino  $\nu_e$  produces at its charged current interaction with matter a secondary electron. By this production a hadronic shower is created. A secondary high-energy electron radiates a photon via bremsstrahlung after a few tens of cm of water/ice. This leads to an electro-magnetic shower. Due to the small distance between the interaction point of the electron neutrino with matter and the creation point of the electro-magnetic shower the production points of both events can normally not be differed in a detector, which leads to a low pointing accuracy. [1, 4, 5]

The NC interaction is independent from the flavor of the neutrino. As it is shown in figure 2.1 in schema (d) no secondary lepton is created by the interaction. So the NC interaction of a neutrino with matter produces a hadronic shower, caused by the interaction process, and

after the interaction there is still a neutrino propagating. Therefore the secondary particles in a NC interaction are produced by the hadronic shower, which contains most dominantly pions, wherein kaons, protons or neutrons emerge in variable fractions. Since the outgoing neutrino always carries a fraction of the interaction energy unobserved away, the error of the reconstructed energy of the primary neutrino increases accordingly. [4]

### 2.3 Detection Principles of Cosmic Neutrinos

The scope of this thesis lies on the high-energy neutrino astrophysics. Hence the goals of the detection of cosmic neutrinos are to determine the direction where the neutrino is coming from and to measure the energy of the neutrino. In face of the fact that neutrinos have a very small cross section a direct measurement of neutrinos is technically not realizable. Therefore a neutrino detector can only measure secondary particles, which are produced by the interaction of neutrinos with matter as already cited in section 2.2. To achieve that the detector must be able to detect the secondary leptons, or respectively effects produced by the secondary particles. The most efficient way to do that is to detect the Cherenkov radiation which is produced by the secondary charged particles while propagating through the medium. [4]

Cherenkov radiation, also called Cherenkov light, is emitted when charged particles are propagating faster than the phase velocity of the medium which through the particle travels. That is, for a medium with refractive index  $n$ :

$$c_n = \frac{c}{n} \tag{2.5}$$

with  $c$  the speed of light in vacuum. The refractive index  $n$  is wavelength dependent. A charged particle which travels with the velocity  $v$  through the detector volume will loose some energy along its path as it polarizes surrounding atoms and molecules and orients dipoles. As soon as the charged particles has passed, the dipoles will go back into their ground state and release energy in form of electromagnetic radiation. If the charged particle is faster than the phase velocity of the medium the electromagnetic waves will interfere to a characteristic light cone with angle  $\theta$ , as it is schematic shown in figure 2.2.

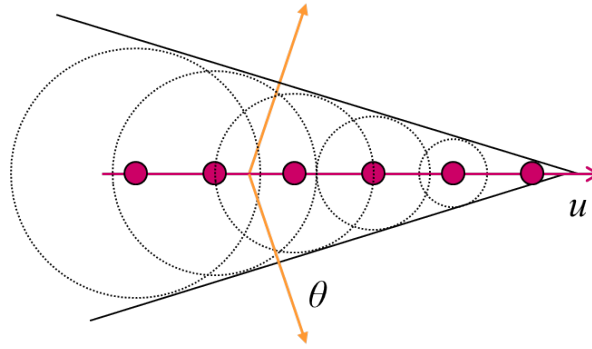


Fig. 2.2: The schematic of Cherenkov light for a moving charged particle with velocity  $u$ . [8]

The correlation between the angle  $\theta$  and the velocity of the charged particle is given by formula 2.6.

$$\cos \theta = \frac{c}{v \cdot n} \quad (2.6)$$

To measure this Cherenkov light the detector contains a three-dimensional array of Photosensors inside the detector volume. Such a Photosensor can comprise one or more Photomultiplier Tubes (PMTs), which are able to detect the photons of the Cherenkov light and convert it into a digital signal. Hence the detector needs to consist of a transparent medium, such as ice or water, so that the photons of the Cherenkov light can propagate in the detector volume. Since the cross section of neutrinos is very small a large detector volume is needed to increase the probability of a neutrino interacting with matter inside the detected volume. Another advantage can be gained by locating the detector at great depths is, as the medium above the detector provides shielding against secondary particles produced by Cosmic-Rays and thus reduces the background noise. [4]

As introduced in section 2.2 the different interaction types of neutrinos interacting with matter result in different event signatures. For the detection of cosmic neutrinos the CC interaction of a muon neutrino with matter leads to a very distinct signature. The secondary muon propagates through the medium creating Cherenkov light along its path, the so-called track signature. Muons have large path lengths in water which means that the muon can travel a long distance through the water without scattering or decaying. Due to this large path length of the muon, large scale detectors achieve the best angular resolution and therefore the direction of the source of the cosmic neutrino can be determined most precisely. [4]

As the amount of Cherenkov light emitted by charged particles created in neutrino interactions is proportional to the deposited energy, which is approximately equal to the neutrino energy for  $\nu_e$  and  $\nu_\mu$  CC interactions, it can be used to set a lower bound on neutrino energies [energy reconstruction icecube]. Thus by measuring the amount of Cherenkov light the energy of charged particles and therefore the energy of the neutrino can be reconstructed. [9, 10]

### 3 The Pacific Ocean Neutrino Experiment

Neutrino detectors have in general, as mentioned in chapter 2.3, the same working principle, which is the instrumentation of a large volume of transparent medium with photosensors to measure the Cherenkov light produced by secondary particles of neutrino interactions. Due to the need of a large volume of an optical transparent medium, ice or water are natural candidates to host such photosensor arrangements. To reduce the background caused by atmospheric muons and neutrinos, which are created by the interaction of Cosmic-Rays with the atmosphere, neutrino detectors are located several kilometers below ground. In the following a short overview of existing neutrino telescopes and ones which are currently under construction respectively in development will be given. [3]

The IceCube detector is located at the Amundsen-Scott south pole station and uses glacial ice as detector medium. The detector has an overall instrumented volume of about one cubic kilometer and hosts in total 5160 Digital Optical Modules (DOMs) arranged on 86 strings, which are deployed in a depth between 1450 and 2450 meter below the surface. DeepCore is a sub-array within IceCube specifically designed for low energy detection of neutrinos around 100 GeV. The DeepCore array consists of 8 strings with respectively 60 narrower spaced DOMs. The detection arrangement is completed by IceTop, which consists of 162 ice-filled tanks instrumented with DOMs. IceTop serves mainly as a veto of down-going muons, but also for studies of PeV gamma rays and radiation effects of solar flares. [11]

KM3NeT is still under construction and is being deployed at three different locations in the Mediterranean Sea and acts as a network of neutrino telescopes. The specific sites are offshore Toulon, France, Capo Passero at Sicily, Italy and Pylos, Greece. Its design and locations in the Mediterranean Sea are optimized for the search of Galactic neutrino sources. The final network of neutrino telescopes will instrument a total volume of around  $3 \text{ km}^3$ . [12, 13]

The Baikal Gigaton Volume Detector (Baikal-GVD) is another neutrino detector currently under construction. As KM3NeT it is located in the northern hemisphere, situated at Lake Baikal in Russia. The concept of Baikal-GVD follows a clustered structure, whereas one cluster holds 288 Optical Modules (OMs) on 8 vertical strings with an inter-string distancing of 60 m and a spacing between clusters of around 300 m. The completion of the first 8 clusters which provide an instrumented volume of  $0.4 \text{ km}^3$  was planned for 2021. [14]

The P-ONE is currently under development. Neutrino telescopes are most sensitive to the horizon of the detector vertex due to the background of atmospheric muons and neutrinos and the opaqueness of the earth for high energy neutrinos. Therefore P-ONE is planned as complementary telescope to cover in combination with the other neutrino telescopes nearly the entire sky for transient events. P-ONE will be located at the Cascadia Basin in the North-East Pacific 200 km offshore Vancouver. There, Ocean Networks Canada (ONC) hosts two large cable ocean observatories, the North East Pacific Time-series Underwater Networked Experiment (NEPTUNE) and the Victoria Experimental Network Under the Sea (VENUS). NEPTUNE comprises five nodes over the Juan de Fuca tectonic plate, which serve as connection points for various kinds of experiments. One node is located at the Cascadia Basin and is selected to host P-ONE. This is one of the major advantages of P-ONE, the cable infrastructure already exists and data transmission to shore-station is established. P-ONE is planned as multi-cubic

kilometer neutrino telescope with a final detector volume of around  $3 \text{ km}^3$ . As shown in figure 3.1, the current concept comprises 7 clusters with 10 mooring lines each. Each mooring line will include 20 optical modules of two different types: an optical module and a calibration module. P-ONE is designed to detect neutrinos with an energy beyond 1 TeV, while the focus is set on the detection of horizontal events. [3, 15]

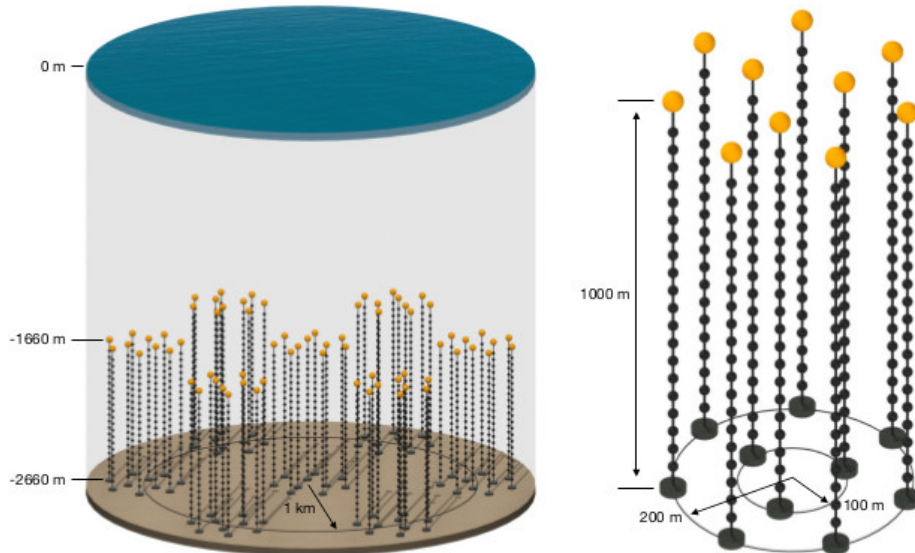


Fig. 3.1: Sketch of the planned P-ONE detector, the preliminary design consists of 7 clusters with 10 mooring lines each, wherein each mooring line comprises 20 modules. [16]

### 3.1 P-ONE-1

Currently the development of P-ONE-1, the first complete prototype line of the final detector, is in full progress. A first concept of P-ONE-1 is shown in figure 3.2, where the amount of the modules depicted was reduced to 10 instead of 20 for graphical reasons. This line aims to be the blueprint for the upcoming P-ONE mooring lines. At the moment the focus lies firstly on the development and construction of the optical modules, which will be able to detect Cherenkov light produced by secondary particles of the interaction of neutrinos with matter, together with the mechanical mounting structure of the modules to the mooring line. Secondly, the deployment strategy is being developed together with the necessary mechanical deployment support structures. Each P-ONE mooring line is planned to have a length of 1000 m and will comprise 20 modules. Of the 20 modules around 16 are planned to be optical modules and around 4 to be calibration modules. The modules will be introduced in more detail at the end of this chapter. [17]

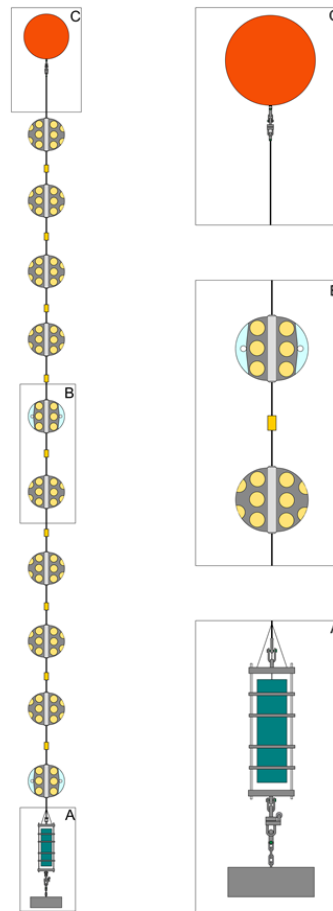


Fig. 3.2: Preliminary schematic of P-ONE-1 consisting of an anchor, a buoy, and the optical and calibration modules. In contrast to the sketch it is intended that each mooring line comprises 20 modules. [17]

### 3.1.1 P-ONE Optical Module

The P-ONE Optical Module (P-OM) is designed to achieve good performance in detecting Cherenkov light produced by secondary particles of the interaction of neutrinos with matter. Therefore it possesses a multi Photomultiplier Tube (PMT) configuration, wherein each PMT has a diameter of 3.1". A first conceptual drawing of a P-OM is shown in figure 3.3. The P-OM consists of two glass hemispheres which are connected to a titanium head ring. This titanium head ring is designed to hold the mounting mechanism of the P-OM with the electro-optical-mechanical backbone cable. The volume inside the glass hemispheres and the titanium head ring can be used to arrange the PMTs and the readout electronics as well as other desired

sensors and electronics. [17]

PMT candidates have been evaluated at the University of Alberta and the Technical University of Munich. The tests included measurements of the dark rate, angular acceptance, transit-time and transit-time-spread, gain, single photo-electron resolution and quantum efficiency. These tests are executed in a dark box using a laser and a diffuse light source, wherein the tested PMT is mounted on two rotatable stages to perform angular dependent measurements. A tender process for the PMT candidates was performed at the end of 2021. One of the most important criteria of the optical module is its effective photosensor area. As a full surface coverage of the glass spheres is technically not possible, the additional implementation of reflective cones around the PMTs are the most efficient way to increase the effective instrumented area. To achieve this and to get the PMTs optically coupled to the glass housing pre-moulded gel pads are currently tested. On one hand this gel pads have the characteristics to act as reflective cones, if an incident photon is in the total internal reflection regime. On the other hand a photon, which does not hit the PMT, can traverse the gel pad and can be detected by a neighbouring PMT. [17]

### 3.1.2 P-ONE Calibration Module

Around four P-ONE Calibration Modules (P-CAL) will be mounted at each mooring line of the P-ONE telescope. The P-CALs will be used to constantly monitor the optical properties and the geometry of the P-ONE sensor arrays, in order to calibrate variations in the optical properties, sedimentation effects and geometry. Therefore the calibration modules emit light pulses in the order of ns, which are detected by the surrounding P-OMs, facilitating the measurement of light attenuation via the flash intensity. The P-ONE collaboration intends to develop a system that allows one to base the entire geometry calibration on this module, exploiting the timing properties of the system. The P-CAL will be designed in a way, that the calibration electronics and supplementary mechanical parts will be enclosed in the same instrument housing as the P-OMs. This provides a seamless integration to the mooring line, simplifies the design and reduces deployment complexity and technical challenges. To prevent blind spots inside the instrumented detector volume the inte-

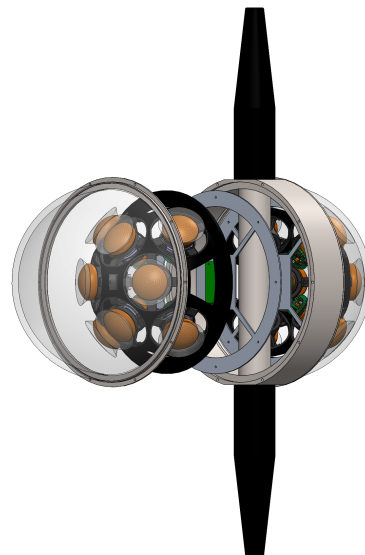


Fig. 3.3: Current concept of the P-ONE optical module. It consists of two 17" glass hemispheres and a titanium head ring and embraces up to 16 PMTs arranged inside the housing together with the readout electronics of the PMTs. Figure kindly provided by Christian Spannfallner.

gration of additional PMTs into the P-CAL is currently planned, as it is shown in figure 3.4. By doing so, it must be ensured that an isotropic emission profile is maintained and the PMTs are not being damaged by the bright light flashes.

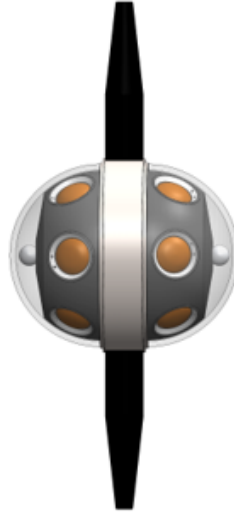


Fig. 3.4: Current concept of the P-ONE calibration module hosted in the standard housing used to constantly monitor the optical properties and the geometry of the P-ONE detector. Next to the calibration hardware also PMTs will be arranged inside the housing to avoid blind spots in the detector volume. Figure kindly provided by Christian Spannfellner.

## 3.2 Pathfinder Missions in Cascadia Basin

To investigate the optical properties at the Cascadia Basin, two pathfinder missions have been deployed. The first one is the Strings for Absorption length in Water (STRAW), deployed in summer 2018, and the other one is P-ONE second pathfinder mission (STRAW-b), which was deployed in fall 2020. Both missions are designed to measure the attenuation length, background rates as well as internal pressure and humidity, magnetic fields and acceleration of the modules. [15]

### 3.2.1 Overview about the Pathfinder Missions

#### Strings for Absorption length in Water

STRAW is built up of two 145m tall instrumented mooring lines, which consist of three Precision Optical Calibration Modules (POCAMs) and five optical modules (sDOM). A technical drawing of the STRAW mooring lines is shown in figure 3.5. It is operating reliably for more than three years with a duty cycle of 98%. Since its deployment in spring 2018 the STRAW mission has

achieved the preliminary assessment of the attenuation length regarding the wavelength of the light, as well as the background rate caused by bioluminescence and the decay of  $^{40}\text{K}$ . [1, 18]

The attenuation length is at 450 nm about 28 m similar to other sites like at KM3NeT, whereas at lower wavelength the values appear reduced to the expected ones [19]. A possible explanation is the fact that STRAW is located quite close to the ground, whereby a more significant sediment dissolution is likely. It is anticipated that the attenuation length is dominated by the absorption of the water, whereas scattering of photons seems subdominant. The second very important target of the STRAW mission is the measurement of the background, caused by both bioluminescence and the decay of  $^{40}\text{K}$ , wherein in chapter 3.2.2 the background of bioluminescence will be outlined in more detail. The continuous noise floor of the decay of radioactive isotopes occurring in sea salt as the  $^{40}\text{K}$  was measured in agreement with the salinity measurement of ONC and was at a value as expected. [3, 15, 18]

### STRAW-b

After the successful deployment of STRAW, the next goal was the verification of the attenuation length and further background measurements. For this purpose STRAW-b was developed. It consists of a roughly 450 m tall mooring line, which comprises in total ten modules. Each module is housed in a 13" high-pressure resistant glass sphere. Three of the ten modules are standard modules, which are able to measure the pressure, temperature and humidity inside the modules and host magnetic field sensors and accelerometers. Two Light Detection and Ranging Modules (LiDAR) aim to measure the scattering length. The muon tracker module is designed to measure atmospheric muon rates, which represent one of the main sources of background. Additional there are two PMT spectrometer modules, which are capable of measuring the spectrum of bioluminescent light in order to improve the background analysis and provide useful information about the bioluminescence burst emission mechanisms. To complement the measurements of the PMT

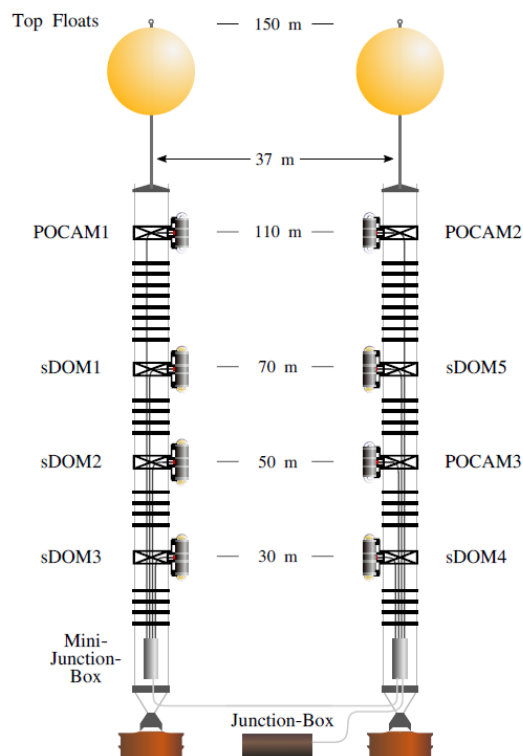


Fig. 3.5: The STRAW mooring lines are two 150 m high mooring lines comprising together 3 POCAMs and 5 sDOMs as well as a Mini-Junction-Box and a buoy at each line. The STRAW mooring lines are designed to characterize the optical properties at Cascadia Basin. [15]

spectrometer the mini spectrometer is configured to measure high-intensity bioluminescence bursts. Finally there is the Wavelength shifting Optical Module (WOM) as a contribution from the University of Mainz, which has been developed for the IceCube Upgrade and is optimized for the detection of UV photons. [15]

The arrangement of the different modules along the mooring line is displayed in the schematic of STRAW-b, shown in figure 3.6.

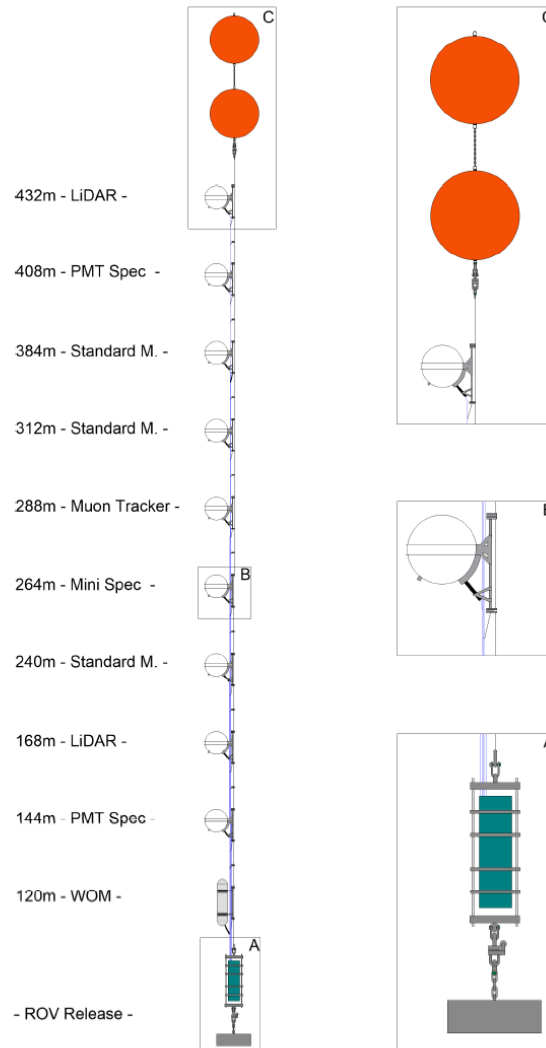


Fig. 3.6: The STRAW-b mooring line is roughly 450 m tall and comprises two buoys, an anchor and 10 module housings, wherein the modules are fitted with different components to characterize the physical conditions at Cascadia Basin. The STRAW-b Pathfinder has three standard modules, two PMT spectrometers, two LiDARs, one muon tracker, one mini spectrometer and one WOM. [15]

### 3.2.2 Background Measurement of Bioluminescence

Next to the measurement of the attenuation length, the second important target of the Pathfinder missions was the characterisation of the background at Cascadia Basin. Next to the background of atmospheric muons and neutrinos, which is present in nearly every neutrino detector, also the decay of  $^{40}\text{K}$  and bioluminescence contribute to the background in the deep-sea. Both are ambient background sources which only exist in water based neutrino telescopes and not in detectors which are located in ice, like IceCube.

Bioluminescence is generally the emission of visible light by a living organism, which is a result of a natural chemical process after a mechanic, electric or light stimulation of the organism. There can be two kinds of bioluminescence differed: The steady bioluminescence is related to the presence of luminescent bacteria that emit steady homogeneous diffused light, varying of a time scale of hours or days. Whereas the bursting bioluminescence is characterized by intensive light bursts that can reach frequencies up to MHz and can last from a few tenths of a second to a few tens of seconds. These bursts are mainly correlated with water currents, wherein the phenomenon can be seasonal or it can happen also when water current values are relatively small and other peculiar environmental conditions occur, like dense water formation events e.g. due to the sinking of cooler and more dense water. [1]

To characterize the background rate caused by bioluminescence the STRAW-b is able to measure the bioluminescence activity emission in deep ocean environmental conditions at Cascadia Basin. Therefor STRAW-b comprises three spectrometer modules. [1]

### 3.3 Possible Measurements of Deep Ocean Parameters in Correlation to Bioluminescence Measurements

In face of the ability of the optical modules of the pathfinder missions to detect the light emitted by bioluminescence, the possibility to record other environmental data can be useful. Recording data like the salinity, temperature and water currents can be helpful for analysing and understanding the events of bioluminescence and exploiting if there is a correlation between different environmental parameters and the light emitting events of bioluminescence. As the optical and calibration modules of the P-ONE detector will also be able to detect visible light which is emitted by bioluminescence the P-ONE detector could be also used to host such environmental sensors. This could provide a basis for a long term detection and analysing of bioluminescence events in correlation to environmental parameters, like temperature.

## 4 Development of Deep Ocean Temperature Measurement Facilities for P-ONE

Currently the development of P-ONE-1 is in full progress. The general project target of the P-ONE-1 is the construction and deployment of a P-ONE mooring line as a first installation of the final P-ONE detector. For that P-ONE-1 shall be the blueprint for the following mooring lines and the working principle and the deployment technique shall be verified. As introduced in section 3.3 the ability of the optical and calibration modules of the P-ONE detector to monitor bioluminescence events left open the opportunity to implement environmental sensors to the modules in order to measure deep ocean parameters, like sea temperature. Due to this arising infrastructure of the P-ONE detector there is the potential to monitor the deep sea temperature in correlation to bioluminescence events and long-term temperature changes of the deep sea in relation to the global warming. Therefor the temperature sensor is planned to be in direct contact with the water, which would be a new type of installation for this project since all other installation has been always encapsulated. In this chapter the research and selection for possible temperature sensors as well as the development of the readout electronics for the temperature sensors will be shown. Additionally tests for the characterisation of the different temperature sensors will be described and the results of the tests will be presented.

### 4.1 Research and Selection for Possible Temperature Sensors

It is aimed to identify temperature sensors with the following requirements. These conditions base on the circumstances which are given by the infrastructure and location of the P-ONE mooring line.

- One of the most important things is the temperature range a sensor has to cover. The P-ONE detector will be located at the deep ocean at Cascadia Basin and the expected temperature will be between  $2^{\circ}\text{C}$  and  $4^{\circ}\text{C}$  [20, 1]. Therefore a temperature sensor should cover at least the range of  $-2^{\circ}\text{C}$  to  $15^{\circ}\text{C}$ .
- Also the resolution and accuracy of the temperature sensor in this range is very relevant. In a first approach the requirement of the resolution was set to  $1\text{ m}^{\circ}\text{C}$  with an accuracy of about  $1\text{ m}^{\circ}\text{C}$  to  $10\text{ m}^{\circ}\text{C}$ .
- Additional the long-term drift of the sensors is important. Even if a temperature sensor has a excellent accuracy and resolution, these conditions have to be met even after several years as the P-ONE detector is designed to last a minimum of 15 years. So the drift of the sensors over time has also be taken into account.
- Next to the temperature related conditions also electronic requirements have to be made due to the limited power available for the P-ONE detector. Hence the drawn current and overall power consumption of the sensor should be as low as possible. The requirements were set to the low  $\mu\text{A}$  region if the temperature sensor is in normal operating mode.

- Since the supply voltage of the modules of the mooring line of the P-ONE detector is currently not determined, the temperature sensor should be able to be operated by a supply voltage of 3.3 V to 5.5 V.
- As the temperature sensor will be mounted at the modules of the mooring line the dimensions of the sensor are also quite important. Hence the dimensions of the sensor should be as small as possible ensure a safe deployment and prohibit damage to sensors and modules. To achieve this a maximum length of 5 cm for the whole temperature sensor arrangement outside the module was set.

The working principle of the temperature sensor was not part of the conditions for the research, rather in the final selection of the sensors for the testing one digital sensor and one analog sensor was chosen to have a comparison in the functionality.

The research turned out to be more difficult than expected as there have been no temperature sensors found which satisfied all requirements which have been set initially. In table 1 a selection of temperature sensors after the research are listed, wherein the conditions which the sensor does not meet are mentioned in the column "Requirements not fulfilled".

<b>Designation of the Sensor</b>	<b>Requirements not fulfilled</b>
LMT70 Precision Analog Temperature Sensor	temperature accuracy
SBE 3Plus Oceanographic Temperature Sensor	dimensions
Fast OEM Temperature sensor with high resolution	dimensions
MLX90615 Infra Red Thermometer	temperature accuracy
SBE 38 Digital Oceanographic Thermometer	dimensions
TMP 117 Digital Temperature Sensor	temperature accuracy
PPL1 Platinum Resistance Thermometer	dimensions, temperature accuracy
Starmon Mini Durable Underwater Temperature Logger	dimensions
P0K1.232.4W.K.010 Platinum Sensor with Wires	temperature accuracy

Tab. 1: Selection of considered temperature sensors for the usage as a long-term temperature monitoring device in the P-ONE detector, wherein the requirements of this section 4.1 which are not fulfilled by the sensors are listed in the right column.

Hereby the listed sensors in table 1 are the best results of the research for proper temperature sensors. As it can be seen in table 1 all sensors which are listed don't fulfill all requirements, which were set up. Generally the problematic condition is either the temperature accuracy or the dimensions of the sensor. So if the selected sensor meets the requirement of small dimensions its accuracy is not high enough, if the selected sensor meets the requirement of the temperature accuracy, its dimensions are much too large. This demanded an increase of the limits of temperature related conditions to a minimum resolution of 10 m°C and an accuracy of 100 m°C. This leads consequently to a lower performance of monitoring the sea temperature, but it has been proven that even with this accuracy of temperature measurements long-term trends of the ocean temperature in the mK range can be detected and analysed [21, 22, 23, 24, 25]. Based on this

new adapted requirements for the temperature sensors three different sensors were selected:

- the Star-Oddi Starmon Mini Temperature Recorder
- the TMP117AIDRVR Digital Temperature Sensor, and
- the P0K1.232.4W.K.010 Platinum Sensor with Wires.

In the following these temperature sensors are more precisely characterized and the reasons for their selection are explained.

#### 4.1.1 Starmon Mini Temperature Recorder

The Starmon Mini Temperature Recorder is a water temperature data logger from the company Star Oddi. It has a form of a cylinder with a diameter of 25 mm and a length of 130 mm, wherein the housing is made of plastic. There is also a version with titanium housing, however in this test the plastic housing was used. The Starmon Mini comprises a long life replaceable battery, a non-volatile EEPROM memory and is capable to measure the temperature with an accuracy of  $\pm 0.025^\circ\text{C}$  with a temperature resolution of  $0.001^\circ\text{C}$ . The sensor has a temperature range from  $-2^\circ\text{C}$  to  $40^\circ\text{C}$ . For usage the Starmon Mini is programmed by the intern software "Sea Star", wherein the starting point of the measurement and the time interval of the measurements can be determined. The measurement data are saved in the intern memory of the Starmon Mini and can be read out with the software after the ending of the measurement. Thus a live measurement of the temperature is not possible with that setup, as the data can only be received after finishing the measurement. [26]

Consequently the disadvantages of this sensor are the large dimensions, which are too high to incorporate the sensor to a module, and the fact that a live temperature detection is not possible as the readout of the measurement data can only occur after the measurement. The Starmon Mini was nevertheless selected to have a high precision calibrated control measurement device for the evaluation test. Additionally the readout electronics as well as the thermal isolation of the sensor tip can be investigated as in section 4.6 introduced.

#### 4.1.2 TMP 117 Digital Temperature Sensor

The TMP117AIDRVR Digital Temperature Sensor is a small Integrated Circuit (IC) digital sensor. It has a maximum operating range from  $-55^\circ\text{C}$  to  $150^\circ\text{C}$ , wherein it has an accuracy of  $\pm 0.1^\circ\text{C}$  in the temperature range of  $-20^\circ\text{C}$  to  $50^\circ\text{C}$ . The power consumption lies at  $3.5\ \mu\text{A}$  at operation and the supply range is from 1.7V to 5.5V. The TMP 117 digital temperature sensor (TMP 117) has a 16-bit resolution what is correspondent to a temperature resolution of  $0.0078^\circ\text{C}$ . The sensor is able to communicate via an I<sup>2</sup>C interface and therefore can be read out by an Arduino board and a computer. Thus the temperature measurement data can be read out live while the measurement is running. The dimensions of the TMP 117 are  $2.1\ \text{mm} \times 2.1\ \text{mm} \times 0.8\ \text{mm}$  and it has 6 connection fields for connection to a board. Connector

1 is for the Serial Clock Line (SCL) of the I<sup>2</sup>C interface communication, connection field 2 is ground (GND), connector 3 is an alert (ALERT) pin, which can be programmed. Connection field 4 is an additional pin (ADD0), which can be connected to ground, connector 5 is responsible for the Power supply (V+) and connection field 6 is for the Serial Data Line (SDA) of the I<sup>2</sup>C interface communication. In the center of the sensor a thermal pad is arranged. [27]

Hence this kind of temperature sensor meets nearly all requirements as introduced in section 4.1, except of the high accuracy condition made in the beginning. But the increased limits of an accuracy of 100 m°C are mostly met. Merely readout electronics have to be developed and connected to the sensor to receive the measurement data. This development is documented in section 4.2.1.

### 4.1.3 P0K1.232.4W.K.010 Platinum Sensor with Wires

The P0K1.232.4W.K.010 Platinum Sensor with Wires (Pt100 sensor) is an analog Platinum Pt100 sensor. This type of platinum sensor works as a temperature dependent resistor. That means that the Pt100 sensor has a resistance of 100 Ω at a temperature of 0 °C and it changes its resistance depending on temperature. Thus the resistance of the Pt100 sensor increases if the temperature increases and decreases if the temperature decreases. The Pt100 sensor has a temperature coefficient of  $\alpha = 0.00385 \text{ K}^{-1}$ , wherein the temperature coefficient is calculated by the formula 4.1:

$$\alpha = \frac{R_{100} - R_0}{100 \cdot R_0}. \quad (4.1)$$

Hereby  $R_0$  is the resistance value in Ω at 0 °C and  $R_{100}$  is the resistance value in Ω at 100 °C. Based on that temperature coefficient the resistance increase of the Pt100 sensor is approximately linear to the temperature increase, wherein the temperature coefficient is the value of the gradient. The temperature range of the Pt100 sensor goes from −200 °C to 400 °C and the temperature accuracy is dependent on the temperature range. The Pt100 meets the tolerance class 1/10 IEC 60751 F0.3 between 25 °C to 55 °C which results in an accuracy of ±0.03 °C in this range. Hence the maximum uncertainty of the Pt100 sensor in the required range is at ±0.05 °C and thereby fulfills the set conditions in section 4.1. The long-term stability is given as < 0.04% at 1000 h at maximal operating temperature, which is a very solid value and fulfills the requirements. The dimensions of the sensor are 2.2 mm × 2.0 mm × 1.1 mm, wherein the connection to the sensor is possible by to silver wires with a diameter of 0.25 mm and a length of 10 mm. [28]

Consequently the Pt100 sensor meets the set requirements mentioned in section 4.1, at which however the resolution of the sensor is dependent of the readout electronics as the Pt100 sensor is an analog sensor.

## 4.2 Development of Readout Electronics for the Temperature Sensors

In the following two sections 4.2.1 and 4.2.2 the development of the readout electronics of the TMP 117 and the Pt100 sensor is described and the chosen applications are explained. For the TMP 117 the readout electronics are based on the details given by the manufacturer [27], whereas the processing of the readout electronics of the Pt100 sensor is based on the research results about effective methods to measure the value of a resistor.

### 4.2.1 Readout Electronics of the TMP117

For the readout of the measurement data of the TMP 117 a printed circuit board (PCB) has been developed. As already mentioned in section 4.1.2 the IC sensor has six connection fields and a thermal field in the center of the sensor housing. The development of this board is based on the information given by the sensors data sheet [27]. The SCL line and the SDA line are used for the communication of the sensor with the controller via the I<sup>2</sup>C interface. Also the ALERT line can be used to program the TMP 117 digital temperature sensor, wherein all three lines are connected via a pull-up resistor of 4.9 k $\Omega$  to the power line. The ground line and the ADD0 line are both connected to the ground and the power supply line V+ is connected to the power supply, whereby V+ is also connected to the ground with a capacitor of 0.1  $\mu$ F for filtering purposes. Due to the layout of the TMP 117 the thermal field in the center of the sensor is orientated towards the board. To accomplish a good temperature measurement of the sensor the board has also a connection field at the position where the thermal field of the sensor will be located, wherein said connection field is plated-through to the other side of the board so that a good heat conduction from the lower side of the board to the thermal field of the sensor is achieved. The three lines SCL, SDA and ALERT have connection pins for a unobstructed connection to the controller via cable lines. The power supply and the ground are connected to a LEMO connector which then can be connected by cable line to the power source. The populated board of the TMP 117 is shown in the appendix in A.2 and A.3. For both the I<sup>2</sup>C interface communication and the power supply an Arduino Nano board is used, which is connected to a computer via USB. For the readout of the TMP 117 the Arduino board is programmed. For each measurement process the programming of the Arduino has been adapted to the desired parameters and the programs are shown in Appendix in section A.4. The programs are written with the Arduino software which uses C and C++ as programming language and then uploaded to the Arduino board. The readout of the measurement data which were transferred from the Arduino board to the computer was carried out by reading out the serial interface of the computer with the software of ExtraPuTTY. This software is able to save the data from the serial interface into a text file which then can be further analysed.

### 4.2.2 Readout Electronics of P0K1.232.4W.K.010 Platinum Pt100 Sensor

As already mentioned in section 4.1.3 the Pt100 sensor is a temperature dependent resistor which increases its resistance value with increasing temperature. Therefore the readout electronic has

to be developed in a way that a good determination of the resistance value of the Pt100 sensor is possible. Finally the concept of the Wheatstone bridge has been chosen to measure the resistance of the sensor. This circuit is based on four resistors, where two resistors are connected in series and the in series connected resistors are connected parallel to each other as it is shown in figure 4.1. An external voltage is installed to the circuit and the voltage between the two parallel arrangements is measured, wherein the voltage is gripped between the two resistors at each parallel circuit.

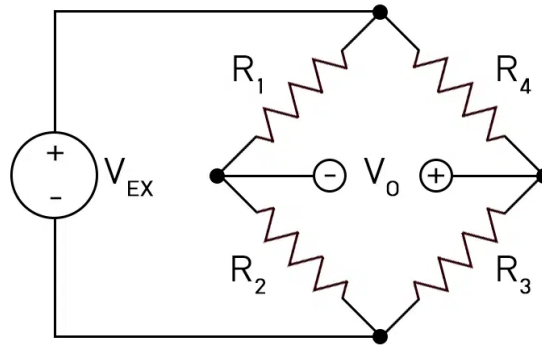


Fig. 4.1: Wheatstone bridge with a power supply voltage  $V_{EX}$ , four resistors, wherein in each case two resistors are connected in series and the in series connected resistors are connected parallel. The voltage  $V_0$  between the parallel connected circuits is measured to calculate the resistance value of one resistor when the remaining resistance values are known. [29]

The relation between the four resistance values is given by the formula 4.2:

$$V_0 = V_{ex} \cdot \left( \frac{R_2}{R_1 + R_2} - \frac{R_3}{R_3 + R_4} \right) \quad (4.2)$$

Hereby  $V_{ex}$  is the external voltage which is installed and  $V_0$  is the voltage measured between the two parallel circuits.  $R_1$  to  $R_4$  are the four resistance values used in the circuit. In general this measurement concept is used to determine a resistance value, for example of the resistor  $R_2$ , by adapting the resistance value of another resistor, in this example  $R_1$ , in that way that the resulting voltage between the two parallel circuits is  $V_0 = 0 \text{ V}$  [30]. This adaption of the resistance value can be achieved by an resistor, which is capable to vary its resistance value as precisely as possible and consequently it is possible to determine its resistance value. If the adaptable resistance value is given, the unknown resistance value of the resistor  $R_2$  can be calculated with formula 4.2. In the present case such a measuring method is not possible since the adaption of a resistor in relation to its value is technically not possible for the provided engineering usage. Nevertheless this method can be use to determine the resistance value even without an adaptable resistor implemented in the circuit. In this case the voltage  $V_0$  between the

two parallel connections needs to be measured. Hence the voltage value  $V_0$  and the voltage value of the external voltage  $V_{ex}$  as well as the known resistance values  $R_1, R_3, R_4$  are known. Based on these known parameters the resistance value of the fourth resistor  $R_2$  can be calculated. This calculation is made in formula 4.3:

$$R_2 = \left( \frac{V_0}{V_{ex}} + \frac{R_3}{R_3 + R_4} \right) \cdot \frac{R_1}{1 - \left( \frac{V_0}{V_{ex}} + \frac{R_3}{R_3 + R_4} \right)} \quad (4.3)$$

By this calculation the resistance value of  $R_2$  can be determined by measuring the voltage  $V_0$ . Hence the Pt100 sensor can be used as  $R_2$  resistance, wherein the sensor changes its resistance value with changing temperature resulting in a change of the voltage  $V_0$ . Consequently by measuring the voltage  $V_0$  the resistance value of the Pt100 sensor can be calculated and the temperature can be determined. For the determination of the temperature formula 4.4 is used, which assumes a linear correlation between the changing resistance value and the temperature change, wherein in section 4.1.3 this assumption is elucidated.

$$\Delta T = \frac{R_T - R_0}{\alpha \cdot R_0} \quad (4.4)$$

Here  $\Delta T$  is the temperature difference to the value  $0^\circ\text{C}$ ,  $R_T$  the measured resistance value of the Pt100 sensor and  $R_0$  the resistance value of the Pt100 sensor at  $0^\circ\text{C}$ , which is  $100\Omega$ . The value of the temperature coefficient  $\alpha$  of the Pt100 sensor is already shown in section 4.1.3 and is  $\alpha = 0.00385\text{ K}^{-1}$ .

For the implementation of the Wheatstone bridge and the readout electronics a PCB has been designed. As the temperature accuracy needs to be very high as introduced in section 4.1 also accuracy of the resistance value measurement needs to be very precise. As the resistance value of the Pt100 sensor is determined on basis of the measured voltage at the Wheatstone bridge, the accuracy of the voltage measurement also needs to be very exact. Since small temperature fluctuations result in small resistance value fluctuations and these result in small voltage fluctuations at the Wheatstone bridge, there is a need to intensify the voltage signal of the Wheatstone bridge to achieve a good temperature resolution. For this purpose an amplifier is arranged on the board which is able to increase the incoming voltage by a defined gain. In this application the amplifier OPA836IDBVR has been used in a non-inverted configuration. The Wheatstone bridge as well as the amplifier receive their individual apply voltages by a power supply unit (PSU) with a direct voltage of  $5\text{ V}$  via a LEMO adapter. The amplified voltage of the Wheatstone bridge is measured by an Arduino Nano board, which is connected to a computer as a controller. The circuit diagram of the Pt100 sensor A.4 is shown in the appendix as well as the table 4, wherein all values of the used components are listed. Several general testings have been done to solve appearing problems. The resulting final working setup for the Wheatstone bridge consists of fixed resistance values for the  $R_1 = R_3 = R_4 = 91\Omega$  and the amplifier resistors have a value of  $R_5 = 24\text{ k}\Omega$  and  $R_6 = 1\text{ k}\Omega$ , which results according to formula 4.5 in a amplification factor of 25 [31]. The populated board of the Pt100 sensor is pictured in A.5 in the appendix.

$$V_{amp} = \frac{R_5 + R_6}{R_6} \quad (4.5)$$

Hence the resistance value of the Pt100 sensor can be calculated by measuring the amplified voltage of the Wheatstone bridge, dividing this value through the amplification factor given by formula 4.5 to get the real voltage of the bridge circuit and calculate the resistance value of the Pt100 sensor with formula 4.3. With the computed value of the Pt100 sensor the temperature can be calculated via formula 4.4. All this calculations have been performed with an excel table.

### 4.3 Experimental Setup for Testing the Temperature Sensors

For the testing of the different temperature sensors, always the same technical setup was used. To be able to characterize the temperature sensors at the required temperatures the testing have been executed inside the Compact Ultra Low Temperature Chamber MC-712R (TC). The TC is able to obtain a temperature range from  $-75^{\circ}\text{C}$  to  $100^{\circ}\text{C}$  inside the test chamber with a temperature fluctuation of  $\pm 0.5^{\circ}\text{C}$  at the location of the temperature control sensor. The TC features the ability to lead electric wires through an outlet in the chamber wall so that only the temperature sensors mounted on the boards are located inside TC, whereas the readout electronics are not effected by the temperature changes while testing. The outlet of the chamber is sealed up with a plug to minimize the temperature losses through the cable outlet. Thus the TC is able to hold its temperature at a constant level within the inaccuracy range of  $\pm 0.5^{\circ}\text{C}$ .

As already mentioned above, the readout electronics aside the components mounted on the temperature sensor PCB are located outside the TC. Hence this components are not effected by the temperature changes of the testing programs. For both the TMP 117 and the PT100 sensor the communication and the readout of the received data occur with with the same Arduino Nano board. This Arduino Nano board is connected to a computer which serves as a controller of the Arduino and as a storage device. The data reveived from the Arduino are read out at the serial interface of the computer (in this case a USB) by the software ExtraPuTTY. After the testing procedure is finished the data are saved in a data file, ready to be imported in the calculation excel table to attain temperature values from the PT100 sensor data. The TMP 117 data is already transmitted in  $^{\circ}\text{C}$  to the computer and saved directly in the data file.

For each testing procedure the temperature sensors have been arranged as close together as possible to minimize the affect of temperature fluctuations, caused by possible different temperature zones inside the TC volume. All temperature sensors have been located inside a circle of a diameter of 6 cm, wherein all sensors are located on the same level of height. For each measurement the tested temperature sensors lie on a layer of foamed material to avoid affects caused by the contact surface of the temperature sensors with bare metal. The arrangement of the temperature sensors inside the TC can be seen in the figures 4.2 and 4.12 for the particular measurements.

## 4.4 Test Procedures and Data Measurements

In the following the different test procedures and the relative data measurements are presented. The series of measurements are introduced chronological as the test series build on one another. In total five different test procedures were executed. The first one was a general characterization measurement to analyze the basic behavior of the different temperature sensors. For this purpose, a 40 hour measurement was performed which is presented in section 4.4.1. The second test series was quite similar to the first measurement and was intended to characterize the temperature sensor in more detail. Hereby the time intervals for each temperature were set shorter than in the first measurement. A detailed discussion of the second data series is made in section 4.4.2. Based on the insights of the second data series the third measurement aimed for the characterization of the response time of the different temperature sensors. For this, large temperature variations between  $-2^{\circ}\text{C}$  and  $20^{\circ}\text{C}$  were performed over a period of 18 hours. This is described in section 4.4.3 in more detail. Based on the promising results of the TMP 117 in previous measurements a measurement with different TMP 117 sensors of different production lines were made to sustain some statistical results. For that a 4 hour 40 minutes measurement was undertaken which is analysed in section 4.4.4. The fifth data series was taken to check the performance of the TMP117 under extreme conditions. Therefor a stress test was performed over 20 hours whereby the sensor had to resist temperatures from  $-50^{\circ}\text{C}$  to  $80^{\circ}\text{C}$ . The results are presented in section 4.4.5.

### 4.4.1 Measurement for the General Characterization of the Different Temperature Sensors

The intention of the first measurement is to get a first characterization of the different types of temperature sensors. The focus lies on the verification of the accuracy of the temperature sensors and if they are working reliably. A program for the TC was made, wherein a temperature range from  $-1^{\circ}\text{C}$  to  $5^{\circ}\text{C}$  has been chosen. Each preset temperature level was continuously hold for 30 min. First the TC was cooled down to  $-1^{\circ}\text{C}$  and then the temperature was increased every half an hour by  $0.2^{\circ}\text{C}$  to the temperature of  $2^{\circ}\text{C}$ . In the range from  $2^{\circ}\text{C}$  to  $4^{\circ}\text{C}$  the temperature was increased by  $0.1^{\circ}\text{C}$  every 30 min. Above  $4^{\circ}\text{C}$  the temperature increase was set again to  $0.2^{\circ}\text{C}$ . After the upper limit of  $5^{\circ}\text{C}$  was reached the program operates mirrored with decreasing temperature until the lower limit of  $-1^{\circ}\text{C}$  is accomplished. Thus the complete data series lasts 40 hours. The program of the TC is shown in table 5 in the appendix. In this measurement all three different temperature sensors which were selected in section 4.1 were tested. The readout of the TMP 117 and the Pt100 sensor has been executed by an Arduino Nano board, which is connected to a computer as controller. For the communication of the Arduino with the TMP 117 via I<sup>2</sup>C and for the readout of the voltage of the Pt100 sensor the Arduino has been programmed. The used program is shown in the appendix in section A.4 and is based on the open source github library of the Arduino community for the TMP 117 [32]. Additionally the program was adapted to fulfill the requirements of the power supply for the TMP 117 and the readout of the voltage from the Pt100 sensor board. The arrangement of the three sensors in the TC is shown in figure 4.2. All sensors are located as close together as

possible as described in section 4.3.

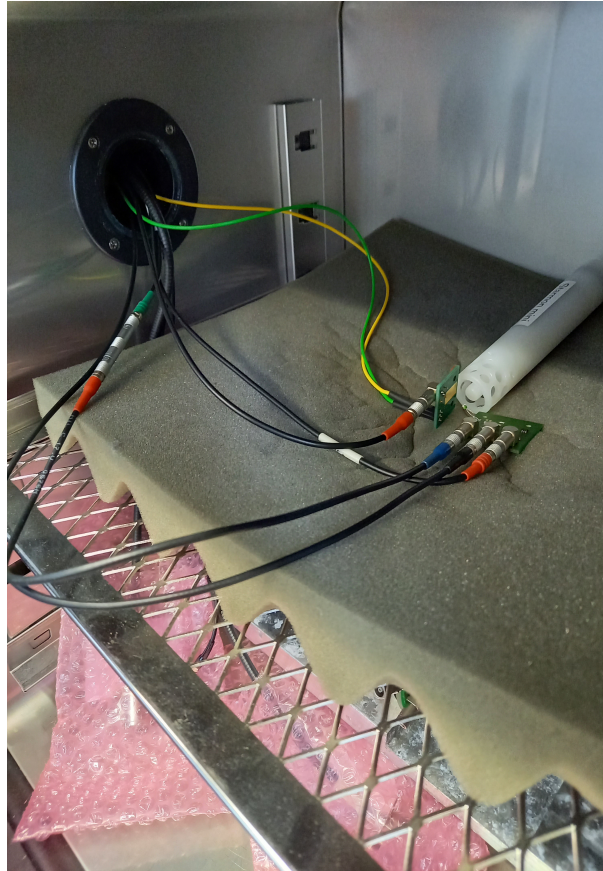


Fig. 4.2: Experimental setup of the different temperature sensors inside the TC for the measurement for the general characterization of the different sensors.

The measurement results are visualized in figure 4.3. The x-axis shows the time in seconds and the y-axis the temperature in  $^{\circ}\text{C}$ . The measurement interval is 30s. It can be seen that the cooling process to  $-1^{\circ}\text{C}$  occurs in quite a short time. In the middle section the temperature steps of the TC are very well visible, as the different gradients for the temperature steps are apparent. In the right edge of the diagram the TC has finished its program and switched off. So the temperature increased until nearly room temperature. The theoretical temperature values of the TC are depicted in green. The blue markers present the measurement results of the Pt100 sensor, which were calculated as in section 4.2.2 introduced. It is obvious that the data of the Pt100 sensor have a big offset and the data points display a strong noise of the sensor. Additionally the Pt100 sensor has a different gradient than the other sensors and as would be expected from the theoretical values of the TC. Hence the offset of the Pt100 sensor is not just of constant behaviour but relies on a more complex function. In face of the strong noise of the Pt100 sensor, a more detailed analysis of the offset have been desisted in the state of measuring.

In red and in black the TMP 117 and the Starmon Mini are shown. It can be seen that both sensors indicate nearly the same temperature over the whole measurement duration. Also, it can be seen that there is an offset between the data points of the last both temperature sensors and the theoretical temperature values of the TC. This results arguably on the inaccuracy of the TC induced by the different location of the temperature control sensor of the TC and the location of the temperature sensors. As the Starmon Mini has been calibrated by the producer it is assumed that the data from the Starmon Mini is correct and can serve as calibration source for the characterization of the other temperature sensors.

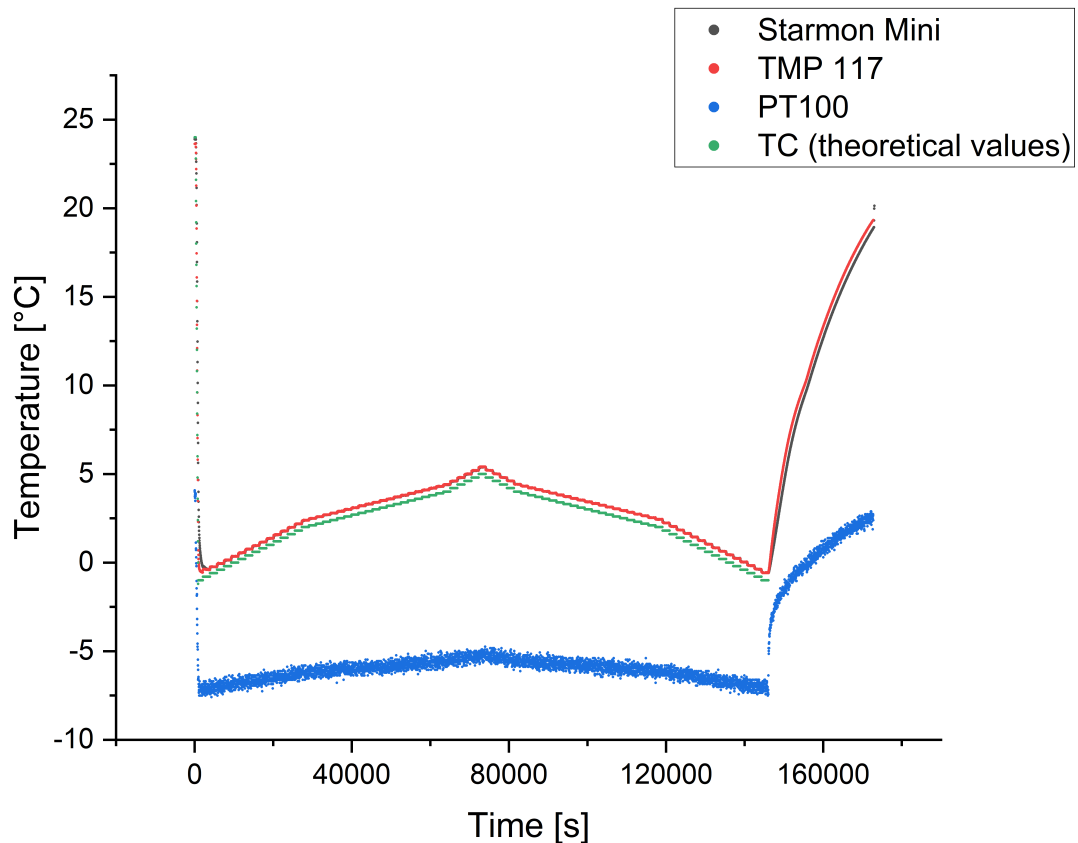


Fig. 4.3: Measurement data from the 40 hour measurement for the general characterization of the different temperature sensors. For more information refer to the text.

To conclude, the TMP 117 provides very accurate data corresponding to the data of the Starmon Mini. Here, hardly a difference between the two sensors is evident, both in accuracy and in noise. In contrast, the Pt100 sensor sent noisy and thus unusable data. The general functionality of the readout electronics of the Pt100 sensor seems to work, as the received data show a temperature dependence and the general shape of the curve follows the other sensors.

#### 4.4.2 Measurement for Detailed Characterization of the Different Temperature Sensors

After the first measurement, a second data series has been taken to get a more detailed characterization of the sensor response in relation to quick temperature changes. Therefore the measurement for the detailed characterization lasts only 40 minutes. In principle the program of the TC resembles the program of the first measurement, where the time for holding a preset temperature was shortened to 1 minute. The temperature range is the same as in measurement one ( $-1^{\circ}\text{C}$  to  $5^{\circ}\text{C}$ ). However, only the increasing temperature steps were measured. The temperature steps for the heating process are the same as in the first measurement. Hence from  $-1^{\circ}\text{C}$  to  $2^{\circ}\text{C}$  the temperature was increased every 60 seconds by  $0.2^{\circ}\text{C}$ . In the range of  $2^{\circ}\text{C}$  to  $4^{\circ}\text{C}$ , the steps size was  $0.1^{\circ}\text{C}$  and from  $4^{\circ}\text{C}$  to  $5^{\circ}\text{C}$   $0.2^{\circ}\text{C}$  again. The program of the TC is shown in table 6 in the appendix. Every 5 seconds a measurement of all three sensors were made to achieve a good time resolution.

The measurement data are shown in figure 4.4, wherein on the x-axis the time in seconds is displayed and on the y-axis the temperature in  $^{\circ}\text{C}$ . Again the theoretical values of the TC are marked in green and represent the program of the TC. In blue the temperature values of the Pt100 sensor are indicated. Again a temperature dependence can be seen as the temperature rises with time, but there is still a massive noise and a strong offset in the data. Also, the gradient of the measurement points is not the same as for the other sensors. Thus the data of the Pt100 sensor is not significant about the temperature, but the data reassures that the working principle of the Pt100 sensor works. In red the measurement data of the TMP 117 is presented. This sensor type affirms its solid performance of the first measurement. The black data points represent the measurement of the Starmon Mini, which is as expected also accurate and stable.

For the more detailed analysis of the measurement data, the section from 500s to 2000s is displayed in figure 4.5. It can be seen that the measurement data of the TMP 117, represented by the red data points, seem to oscillate. This behaviour can not be understood as a signature of noise or inaccuracy of the sensor but can be attributed to the functionality of the TC. When the TC needs to reach a new temperature it can be anticipated that it over-cools respectively over-heats its volume. As in this measurement every 5s a measurement was done a very precise time recording was achieved. Hence the signature of oscillation of the TMP 117 does not belong to the sensors but to the heating procedure of the TC and demonstrates the fast response time of the TMP 117.

In contrast to this just mentioned phenomenon of the TMP 117 the data of the Starmon Mini does not show such behaviour. By comparison to the TMP 117, the Starmon Mini seems to respond slower to the temperature changes. This occurs primarily in the region until 1000s, where the temperature increases every 60s with  $0.2^{\circ}\text{C}$ . With less increasing temperature between 1000s and 2000s the Starmon Mini appears to be able to respond fast enough to the temperature variations. In this second area the data of the TMP 117 and the Starmon Mini are more in agreement with each other. Still both data sets of both the TMP 117 and the Starmon Mini feature an offset related to the theoretical values of the TC. As this emerged already in

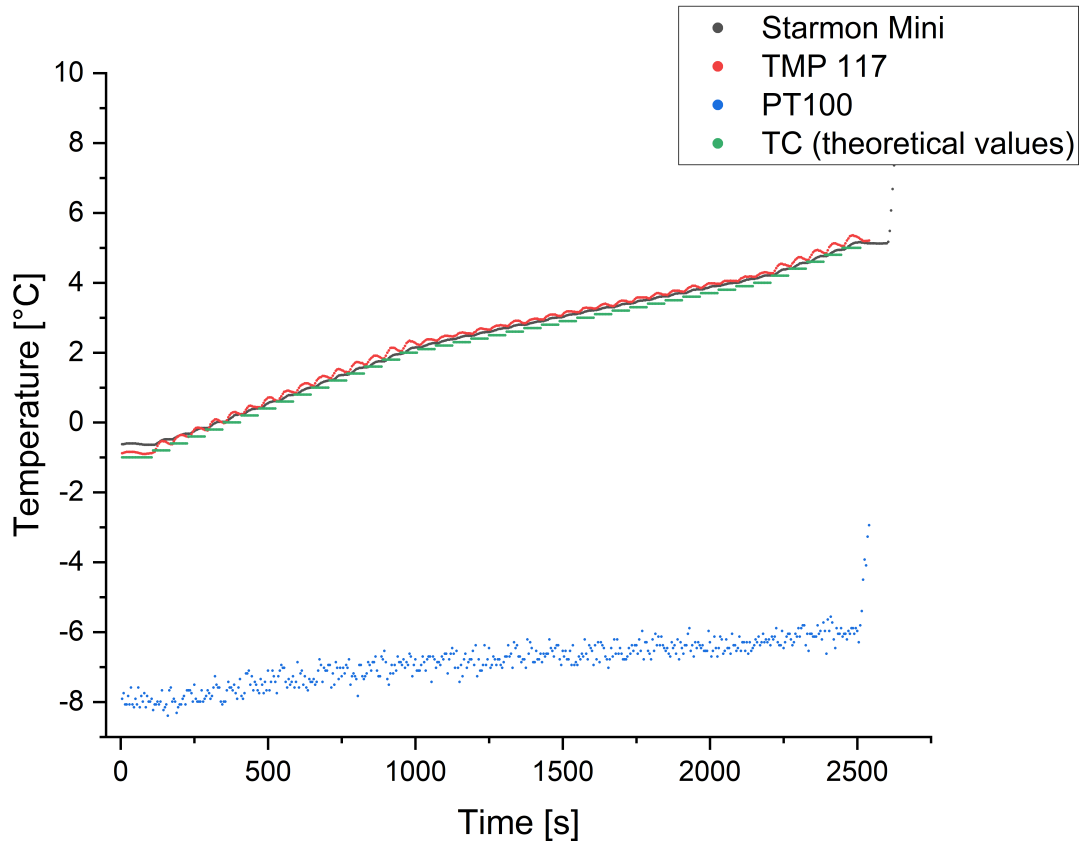


Fig. 4.4: Measurement data from the 40 minutes measurement for the detailed characterization of the different temperature sensors. For more information refer to the text.

the first measurement in section 4.4.1 this offset is more related to the inaccuracy of the TC than to the behaviour of the temperature sensors. Thus this offset is not taken into account for the analysis of this measurement.

Based on this measurement the promising performance of the TMP 117 of the first measurement has been confirmed. In terms of accuracy as well as in response time and low noise the temperature sensor seems to be auspicious. The Starmon Mini indicates a too long response time for this short period measurement. This belongs presumably to its construction as the sensor is arranged inside a plastic housing which provides a shielding effect from the temperature fluctuations. The readout of the Pt100 sensor was again not usable for temperature determination and showed once again massive noise.

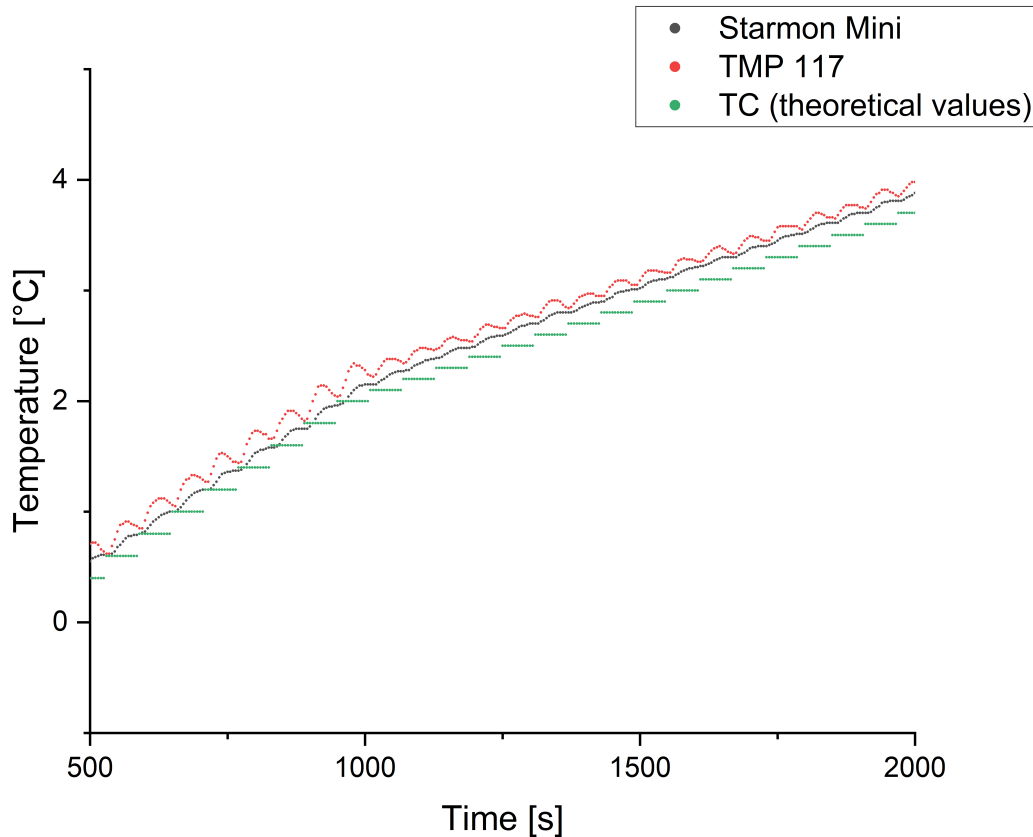


Fig. 4.5: Section from 500 s to 2000 s of the measurement data from the 40 minutes measurement for the detailed characterization of the different temperature sensors. For more information refer to the text.

#### 4.4.3 Measurement of the Response Time of the Temperature Sensors

In the following the measurement of the response time of the temperature sensors will be exemplified. Therefore, a temperature range between  $-2^{\circ}\text{C}$  and  $20^{\circ}\text{C}$  was selected. This range was chosen as it is the maximum range of the Starmon Mini, which is one of the temperature sensors of most interest. The program consists of oscillating temperature changes between the temperature values of  $-2^{\circ}\text{C}$  and  $20^{\circ}\text{C}$ , wherein each present temperature was held for two hours. The program starts with a cooling of the TC to  $-2^{\circ}\text{C}$  and then oscillates between the two mentioned values four times and ends again at a temperature of  $-2^{\circ}\text{C}$ . The program of the TC is listed in table 7 in the appendix. This procedure was selected to characterize quantitatively how fast the different temperature sensors can adapt to the set temperature. The measurement results are shown in figure 4.6, wherein on the x-axis the time in seconds is displayed and on

the y-axis the temperature in °C. In red the data points of the TMP 117 are displayed, in black the measurement points of the Starmon Mini. The data set of the Pt100 sensor is indicated in blue. The theoretical values of the TC are marked in green.

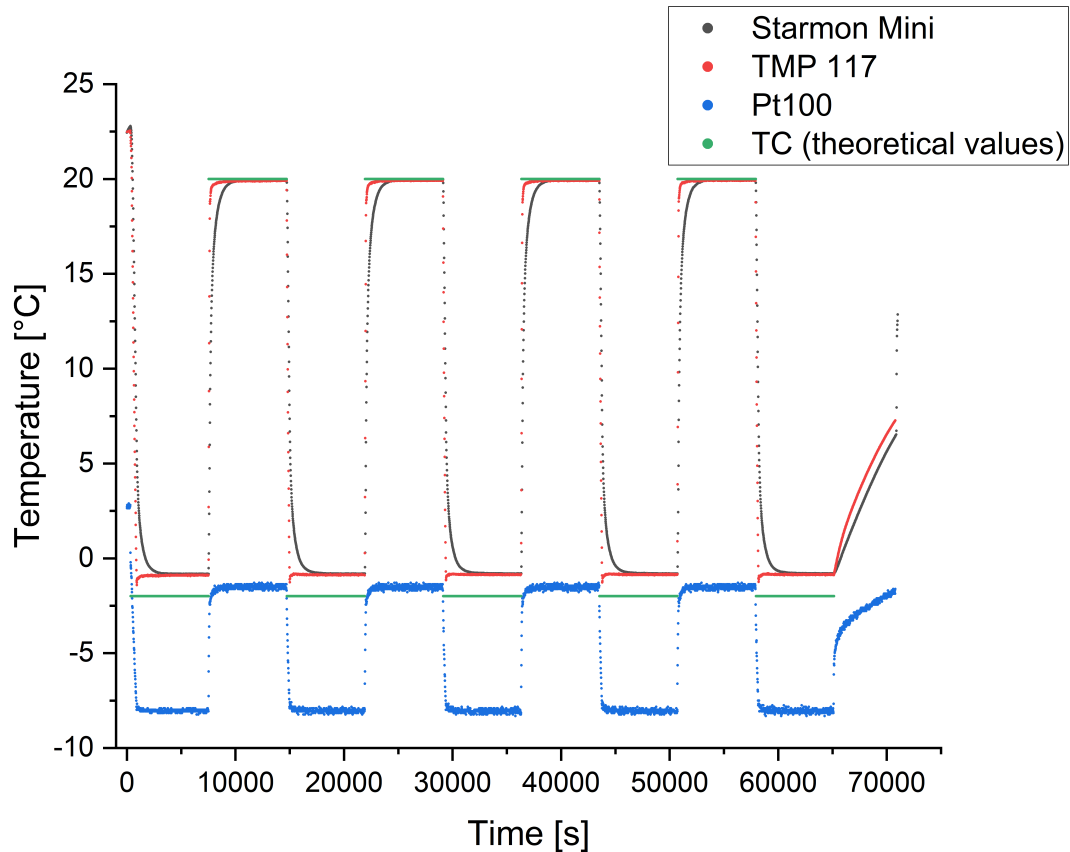


Fig. 4.6: Pictured measurement data of the response time measurement. For more information refer to the text. For more information refer to the text.

The data of the Pt100 sensor has again a strong offset. Also it is noisy at constant temperatures and the offset is not linear, as the difference between the maximal and the minimal temperature is about  $\Delta T = 6.5^\circ\text{C}$  and not as expected  $\Delta T = 22^\circ\text{C}$ . Nevertheless the results substantiate the previous made evaluation that the functionality of the Pt100 sensor is given, but is not accurate enough to deduce a realistic temperature out of the measurement data.

Hence, the focus of the measurement lies on the TMP 117 and the Starmon Mini. Both sensors perform, as expected, very good regarding the temperature accuracy at constant temperature. A major difference can be observed at the response time of the different sensor types. As already seen in section 4.4.2 the TMP 117 responds very fast to temperature changes. The Starmon Mini

does not react as fast, also when it gets close to the preset temperature the adjustment speed of the Starmon Mini decreases. Thus the adjustment curve follows not the step function of the temperature oscillation, but has a more rounded shape when getting to the preset temperature. This can be attributed to the construction of the housing of the Starmon Mini made of plastic and might confirm the assumption made in section 4.4.2.

The short response time of the TMP 117 is also observable at the cooling process of the TC. As already mentioned in section 4.4.2 the TC over-cools the volume when reaching the preset temperature, this effect is especially strong at large temperature changes as they were made in this measurement. This effect was measured by the TMP 117 and causes the small negative peak of around  $0.3^{\circ}\text{C}$  at the end of the cooling process of the TC as pictured in figure 4.6. As in the measurements before there is an offset between the measured temperature of the sensors and the preset theoretical temperature of the TC. This offset is induced by the inaccuracy of the TC temperature control sensor and the different location of the TC control sensor and the tested temperature sensors. That the offset is much stronger at lower temperatures as the preset temperature is  $-2^{\circ}\text{C}$  than at higher temperatures like  $20^{\circ}\text{C}$ .

Thus with this measurement of the response time the made assumption have been validated and the conclusion can be made that the TMP 117 has a much smaller response time than the Starmon Mini. Here it is assumed that this difference in response time is mainly caused by the plastic housing of the Starmon Mini whereas the TMP 117 is just arranged on a readout board as introduced in section 4.2.1.

#### 4.4.4 Measurement of four TMP 117 Digital Temperature Sensors of Different Production Lines

Based on the promising results of the TMP 117 in the previous measurements a next data series has been made to proof these antecedent results. Therefor four TMP 117 of different production lines have been tested to receive some statistical findings about the accuracy of the TMP 117 sensor.

Therefor the program of the TC, shown in the appendix in table 8, was performed. At the beginning the TC was cooled down to  $-2^{\circ}\text{C}$  for 1 hour. Then the temperature was increased every half an hour for  $2^{\circ}\text{C}$  until the temperature of  $4^{\circ}\text{C}$  is reached. Hereupon the temperature was decreased every 5 minutes in  $0.1^{\circ}\text{C}$  steps until  $2^{\circ}\text{C}$  was reached. Hereby a jump of  $0.3^{\circ}\text{C}$  between  $3.5^{\circ}\text{C}$  and  $3.2^{\circ}\text{C}$  has been made due to a mistake in programming the TC. Further the TC cooled the temperature down to  $-2^{\circ}\text{C}$  every 5 minutes in  $0.2^{\circ}\text{C}$  steps.

In figure 4.7 the data of the measurement are shown. In red the data set of the previous used TMP 117 (Mouser 1) is pictured. In black the temperature sensor TMP117AIDRVT (DK1) is indicated and in blue and in green the temperature sensor TMP117MAIDRVT (DK2/1, DK2/2) is presented. Hence, three different temperature sensors from different production batches were used for this measurement to get some comparable data. It can be seen that all sensors follow in general the same curve, wherein there are some offsets between the sensors. Hereby the Mouser 1 sensors stands out because of its overreacting signal. At the cooling from room temperature down to  $-2^{\circ}\text{C}$  a over-cooling is detected by the sensor, wherein the other sensors don't show

such a behaviour. This effect occurs also at other temperature changes even though this effect is strongest at large temperature changes. The remaining temperature sensors behave like expected as they indicate a decelerating approach to the preset temperature of the TC. If this strong effect belongs to the behaviour of the tested TMP 117 digital temperature sensor or if the reason for this effect lies in the location of the sensors inside the TC can not be accounted for with this measurement.

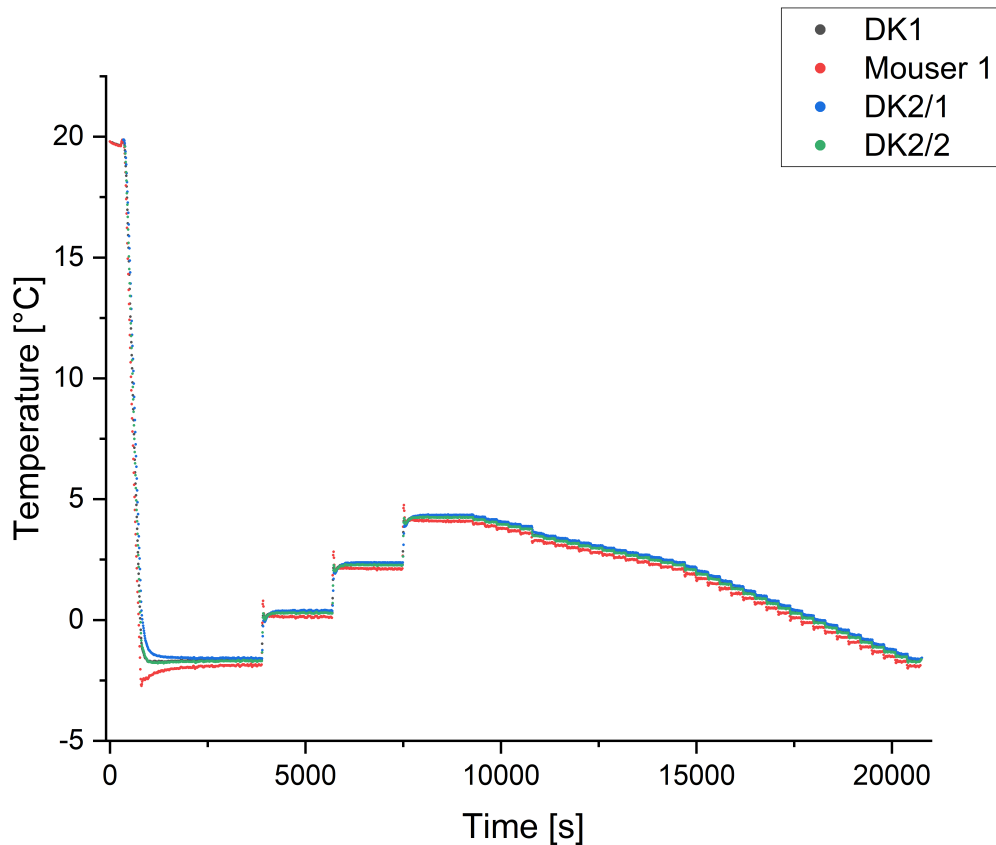


Fig. 4.7: Pictured measurement data of the four TMP 117 digital temperature sensors of different production batches. For more information refer to the text.

As mentioned above there is an offset between the data sets of the different temperature sensors. To determine these offsets two different approaches have been made. In both, the reference values is the temperature data of the Mouser 1 TMP 117. For the first approach the average deviation of the data points of the particular sensors to the Mouser 1 sensor from 2500s to the end of the measurement has been calculated. In the second approach the average deviation of the data points of the particular sensors to the Mouser 1 sensor from 7800 s to the end of the measurement has been computed. These specific intervals were selected to reduce the impact of the cooling

process in which as mentioned before the Mouser 1 sensor shows an strong over-cooling effect. That is why the first approach to calculate the offset of the temperature sensors start at the time of 2500s. The second approach aims for the offset of the sensors in the slow cooling process. Based on this target the calculation of the offset starts at 7800s. To get the average deviation of the data sets at every measurement moment the differences between the Mouser 1 data and the different temperature data of the sensors are calculated. Then the sum of all differences was taken and divided through the amount of data points that have been selected for the offset calculation. The results of the offset calculation are listed in table 2.

	<b>DK1</b>	<b>DK2/1</b>	<b>DK2/2</b>
offset for $t > 2500$ s	0.19 °C	0.28 °C	0.17 °C
offset for $t > 7800$ s	0.21 °C	0.31 °C	0.19 °C

Tab. 2: Results of the offset calculation for the considered time intervals.

The corrected measurement data with the calculated offsets are shown in figure 4.8 for the first approach and in figure 4.9 for the second approach. Hereby the figures present only the time intervals for which the appropriate offset calculation was performed. It can be seen in table 2 that the differences between the two calculated offset values for each temperature sensor are relatively small. Since the temperature difference between a temperature sensor (TS) and the Mouser 1 (M1) sensor has been calculated as  $\Delta T = T_{TS} - T_{M1}$ , the smaller values for the calculation for  $t > 2500$ s can be explained by the over-heating effect of the Mouser 1 sensor. This effect is indicated in figure 4.7 at the temperature changes from  $-2$  °C to  $4$  °C in  $2$  °C steps, where the sensor possesses a short peak. As this over-heating effects are included in the time interval for the first approach of the calculation of the offset they lead to smaller offset values.

In general in both figures 4.8 and 4.9 it is indicated that the correction of the data by the offset values results in good findings. The results of the correction by the offset values are shown in more detail in the cutout of the measurement data in figures 4.10 and 4.11. Thus the differences between the different temperature sensors lie in a constant offset value which can be corrected with low effort. However the Mouser 1 sensor features the over-cooling respectively over-heating effect also at small temperature changes as it is indicated in figure 4.9.

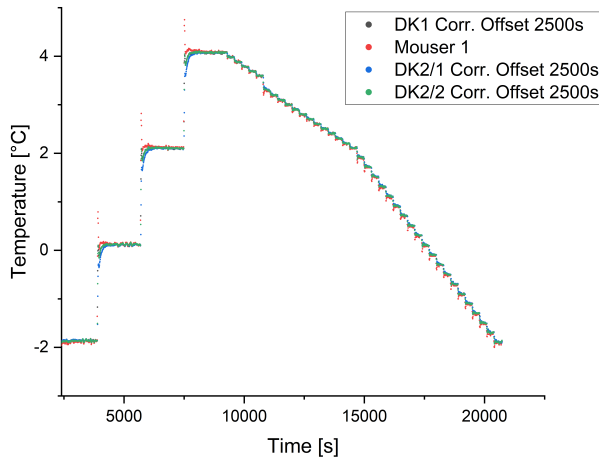


Fig. 4.8: Measurement data of the four TMP 117 digital temperature sensors of different production batches, corrected by the offset values for  $t > 2500$  s.

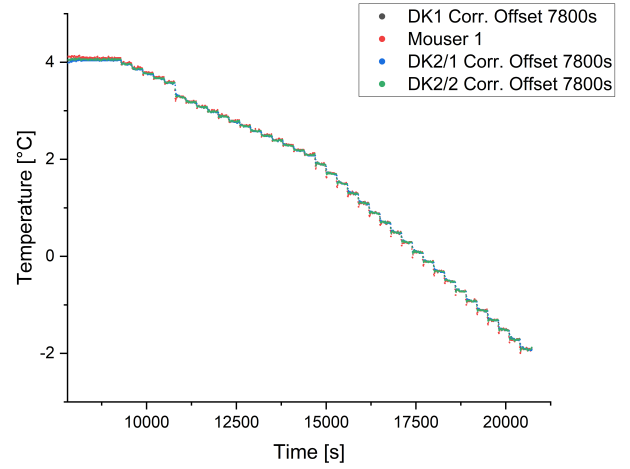


Fig. 4.9: Measurement data of the four TMP 117 digital temperature sensors of different production batches, corrected by the offset values for  $t > 7800$  s.

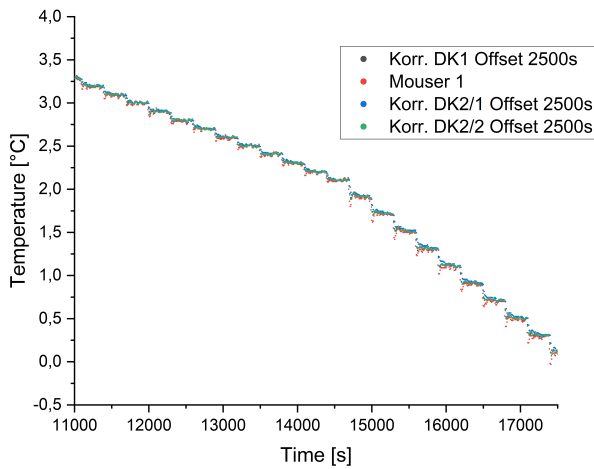


Fig. 4.10: Cutout of the measurement data of the four TMP 117 digital temperature sensors of different production batches, corrected by the offset values for  $t > 2500$  s.

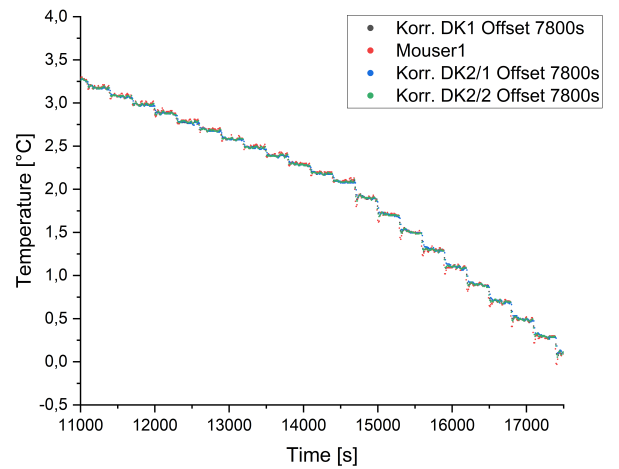


Fig. 4.11: Cutout of the measurement data of the four TMP 117 digital temperature sensors of different production batches, corrected by the offset values for  $t > 7800$  s.

As this effect occurs at every temperature change it is probable that its cause lies preponderant in the behaviour of the Mouser 1 sensor and not in the positioning of the sensor inside the TC. This conclusion is based on the attempt of positioning all sensors as close as possible together, the Mouser 1 sensor is the sensor which is located closet to the TC cooling/warming outlet. The positioning of the sensors inside the TC is shown in figure 4.12.

In general the good results of the TMP 117 of the previous measurements has been confirmed by the measurement of a plurality of four sensors in this experimental procedure. Nevertheless the different TMP 117 sensors have small offset values to each other, while these offsets are of constant behaviour. Hence the offset can be corrected by a calibration of the sensors. In total the corrected data are in good agreement to each other as it is shown in figures 4.8 and 4.9. The Mouser 1 sensor shows over-cooling respectively over-heating behaviour. The reason can not be determined exactly and might be cause by the location inside the TC or the sensor behaviour in general.

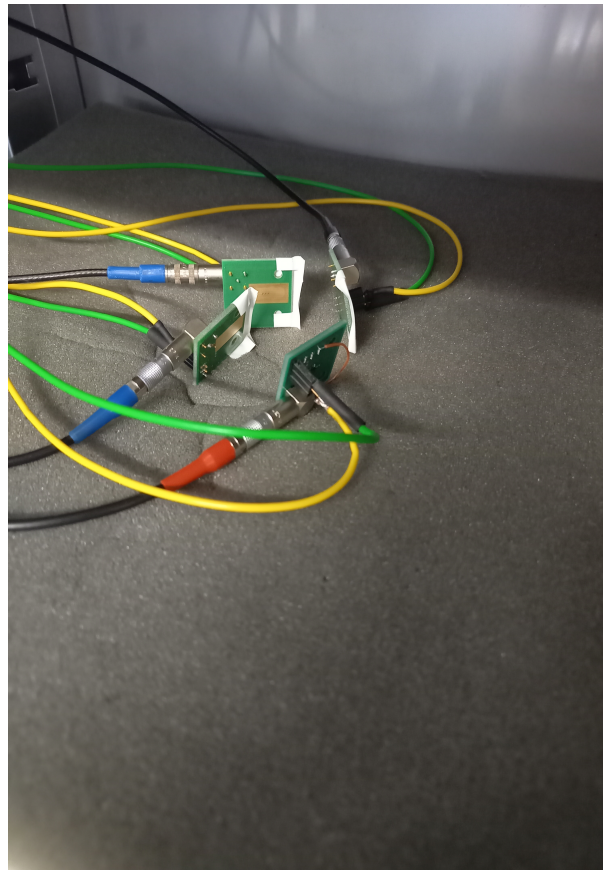


Fig. 4.12: Experimental setup of the measurement of four TMP 117 digital temperature sensors of different production lines. The Mouser 1 sensor is located on the front right, closest to the exhaust of the TC, which is located on the right in this picture.

#### 4.4.5 Stress Test Measurements of the TMP 117 Digital Temperature Sensor

In the final measurement a stress test of the TMP 117 has been performed. The stress test aims for some exceptional conditions for the temperature sensor, which will not appear in the intended usage. In this stress test data are recorded every 30 s. The program of the TC starts with cooling down to  $-50^{\circ}\text{C}$  for 60 minutes. Then every 90 minutes the temperature changes from  $-50^{\circ}\text{C}$  to  $80^{\circ}\text{C}$  and reverse. This temperature changes have been performed so often that in total 5 times  $80^{\circ}\text{C}$  has been reached and in total 6 times  $-50^{\circ}\text{C}$ . Thus the stress part of the measurement ends with a temperature of  $-50^{\circ}\text{C}$ . After that for 30 minutes the temperature of  $10^{\circ}\text{C}$  is hold and for 15 minutes each the temperature of  $5^{\circ}\text{C}$  and  $0^{\circ}\text{C}$  is kept. Finally an accuracy part is performed by holding each temperature for 5 minutes starting with  $2^{\circ}\text{C}$  and ending with  $4^{\circ}\text{C}$ , wherein temperature steps of  $0.1^{\circ}\text{C}$  are used. Hereby the temperature  $3.3^{\circ}\text{C}$  has been skipped by mistake in programming the TC. The program of the TC is shown in the appendix in table 9. The measurement data of the complete stress test are represented in figure 4.13, wherein on the x-axis the time in seconds is displayed and on the y-axis the temperature in  $^{\circ}\text{C}$ . In red the data of the TMP 117 sensor are indicated. It is apparent that the temperature sensor has no problems with high or low temperatures as its data coincide with the preset temperatures of the TC. Also no over-heating and just a very small over-cooling effect is visible, which was based on the information received by the previous measurements not expected. A cause for the absence of this effect in this measurement could be the longer gap between moments of data recording, so that short time effects like over-heating and over-cooling can not be registered. Also a different location inside the TC is a possible reason for the absence of the effect, albeit this seems to be unlikely.

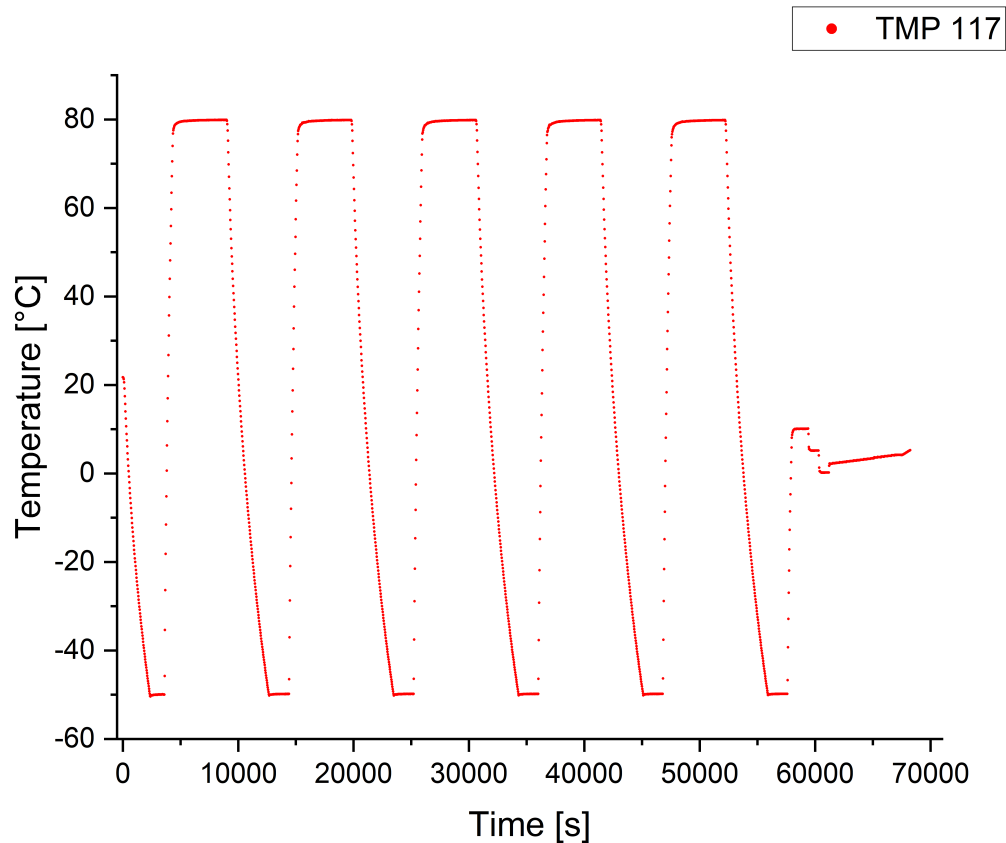


Fig. 4.13: Measurement data of the stress test of the TMP 117 digital temperature sensor.

The section of most interest in this measurement is the part of small temperature changes in the temperature range between 2°C and 4°C. Therefore this particular section is shown in detail in figure 4.14. In the first part preset temperatures of 10°C, 5°C and 0°C are indicated, where a small offset to the theoretical temperature value of the TC is apparent. As this offset has also been registered in the previous measurements it results likely from the inaccuracy of the TC. In the time interval from 61250s to 67500s temperature steps of 0.1°C every 5 minutes are performed. Here the sensor achieves a very high accuracy, where no major deviations from the expected values occur.

These test results show that the TMP 117 digital temperature sensor can achieve a very good accuracy even after a strong thermal strain. Thus the sensor confirms its good performance of the previous measurements.

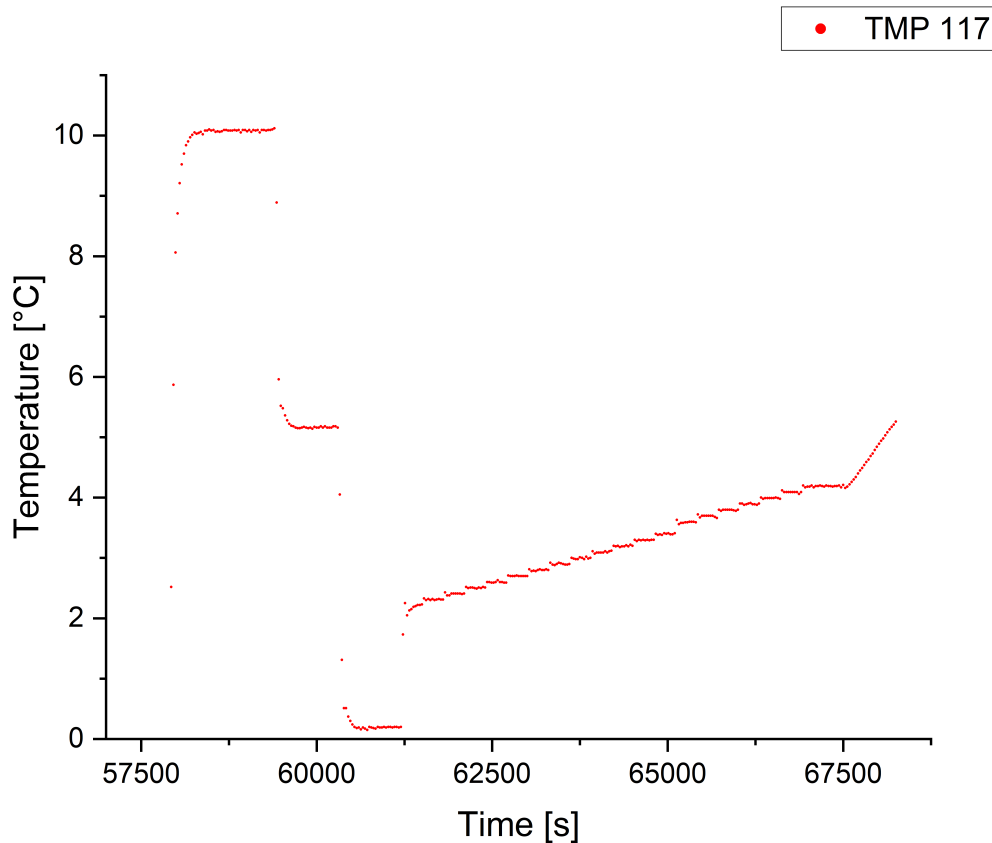


Fig. 4.14: Measurement data of the accuracy section of the stress test of the TMP 117 digital temperature sensor. For more information refer to the text.

#### 4.5 Evaluation of the Measurement Results

The results of the measurements introduced in section 4.4 lead to the valuation that the TMP 117 seems to be a solid candidate for the function as a temperature sensor at the P-ONE. It can perform in the required temperature range and achieves a very good accuracy, which is better than declared in the data sheet of the sensor. To reach this accuracy a precise calibration is needed though, as the measurement of the four TMP 117 digital temperature sensors in section 4.4.4 indicates. The sensor has a short response time as demonstrated in section 4.4.2 and 4.4.3 and can endure heavy strains as proved in the measurement in section 4.4.5. Thus the TMP 117 sensor is a promising candidate for the usage as a temperature measurement facility for the P-ONE-1.

The analog Pt100 sensor demonstrates an insufficient performance in the made measurements. The noise in the data for a constant preset temperature is too intense to determine a precise

temperature as it can be seen in the measurements in section 4.4.1, 4.4.2 and 4.4.3. Also this sensor has a strong non-constant offset, which would make a calibration very elaborate and not constructive. However the readout mode of operation with the appropriation of the Wheatstone Bridge to calculate the temperature dependent resistance value of the Pt100 sensor worked basically. Nevertheless this sensor setup is not suitable for the usage as a temperature sensor. The Starmon Mini performs with the expected accuracy, while its response time is noticeable slower than the response time of the TMP 117 digital temperature sensor as the measurements in sections 4.4.3 and 4.4.2 indicate. The purpose of the Starmon Mini was the verification of the temperature inside the TC as it is an industrial calibrated sensor, which it fulfilled completely. Also the Starmon Mini could be of interest if it belongs to thermal isolation between the sensor and the readout electronics. The study of this is one of the upcoming further steps in the development of a dedicated temperature sensor attachment for P-ONE-1.

#### 4.6 Prospect to Following Proceeding

Based on the previous measurements the TMP 117 is the most promising sensor. Hence further investigations concerning this sensor should be carried out. A specific measurement regarding the cause of the over-heating respectively the over-cooling effect is reasonable, in order to exclude that the cause lies in the behaviour of the TMP 117.

In the further development of a temperature device for P-ONE-1 a new more compact board of the TMP 117 needs to be designed, which meets the small dimensions required as mentioned in section 4.1.

Parallel the processing of a housing which can contain the TMP 117 board should be undertaken, where the housing should be waterproof, pressure resistant and connectable somehow to the module housing of the P-OM. Also the housing should provide a thermal isolation between the module and the sensor readout electronics and the sensor itself to minimize a possible influence on the measured ambient temperature. For the development of the housing of the sensor the technical solution of the industrial temperature recorder Starmon Mini could be helpful. Thus the Starmon Mini should be deconstructed to analyse the technical implementation of the thermal isolation and readout electronics. For the connection between the housing of the sensor and the module housing of P-ONE-1 technical solutions have also to be developed. The connection requires to be waterproof and pressure resistant as well as it has to be able to transmit data and power between the module and the sensor. Additionally the connection needs to be absolutely secure so that if the sensor gets destructed or the sensor housing gets separated from the module the module has to keep functioning without restriction.

Parallel to the development of the mounting, a method for high precision calibration of the TMP 117 needs to be designed. As the measurement of the different TMP 117 sensors in section 4.4.4 shows the industrial calibration of the sensors is not accurate enough to fulfill the set requirements. Therefore a calibration procedure needs to be developed to guarantee a high accuracy of the sensors.

## A Appendix

### A.1 TMP 117 Digital Temperature Sensor

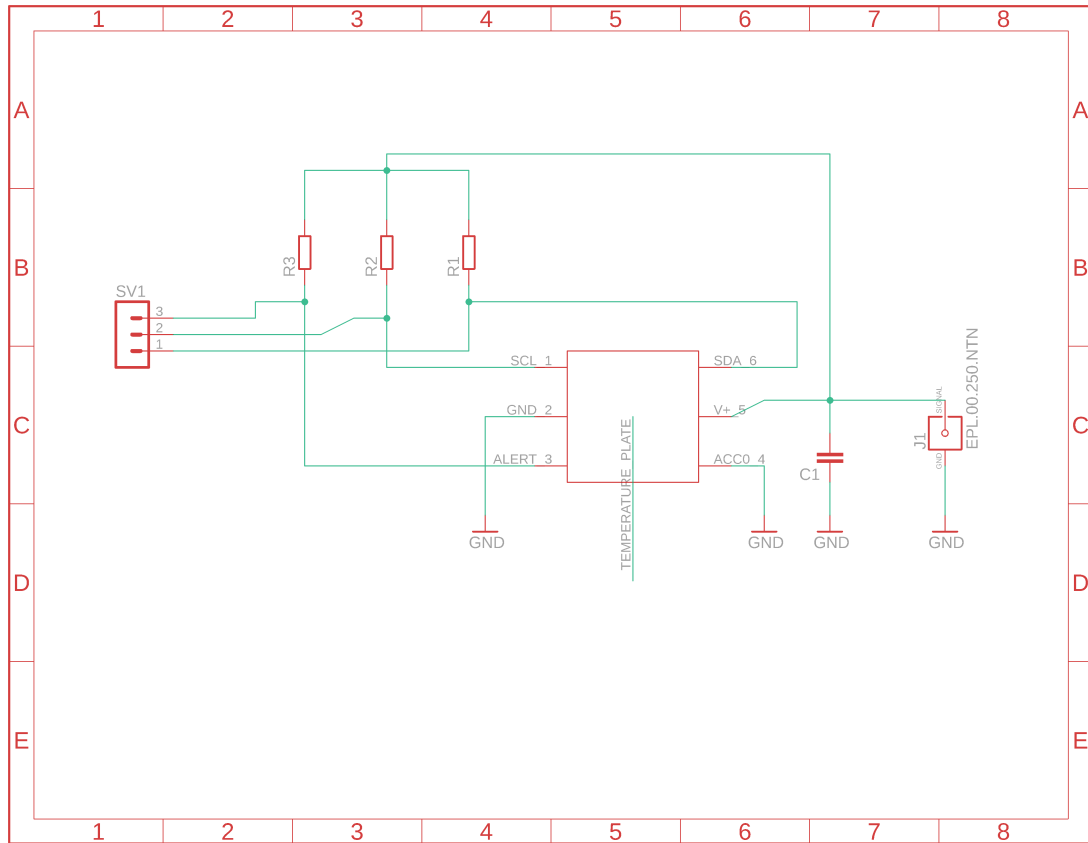


Fig. A.1: TMP 117 readout electronics schematic.

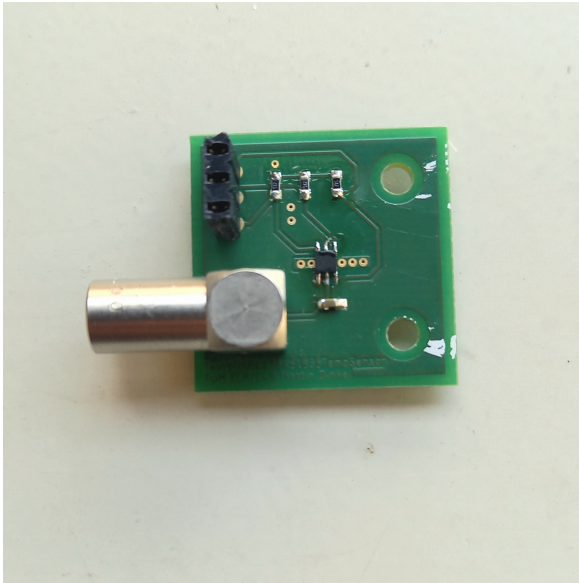


Fig. A.2: Front side of the populated board of the TMP 117.

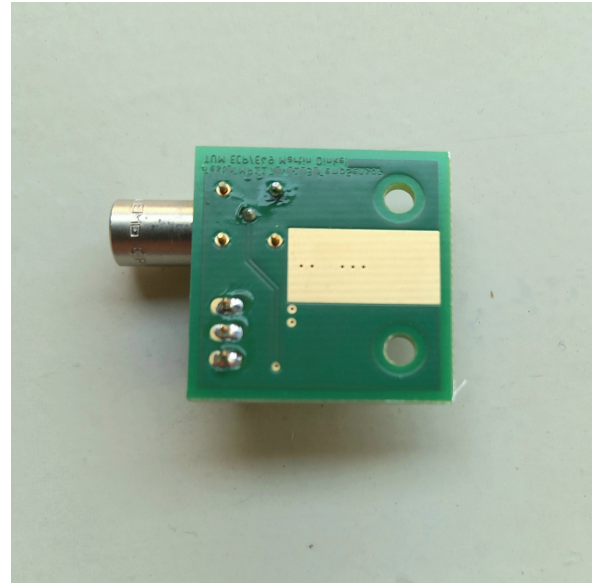


Fig. A.3: Back side of the populated board of the TMP 117.

electronic component	used values
R1	4.9 k $\Omega$
R2	4.9 k $\Omega$
R3	4.9 k $\Omega$
C1	100 nF
SV1	connection pins for I <sup>2</sup> C
J1	LEMO connector for power supply

Tab. 3: Listing of the used values for the electronic components of the board of the TMP 117 digital temperature sensor.

## A.2 P0K1.232.4W.K.010 Platinum Sensor with Wires

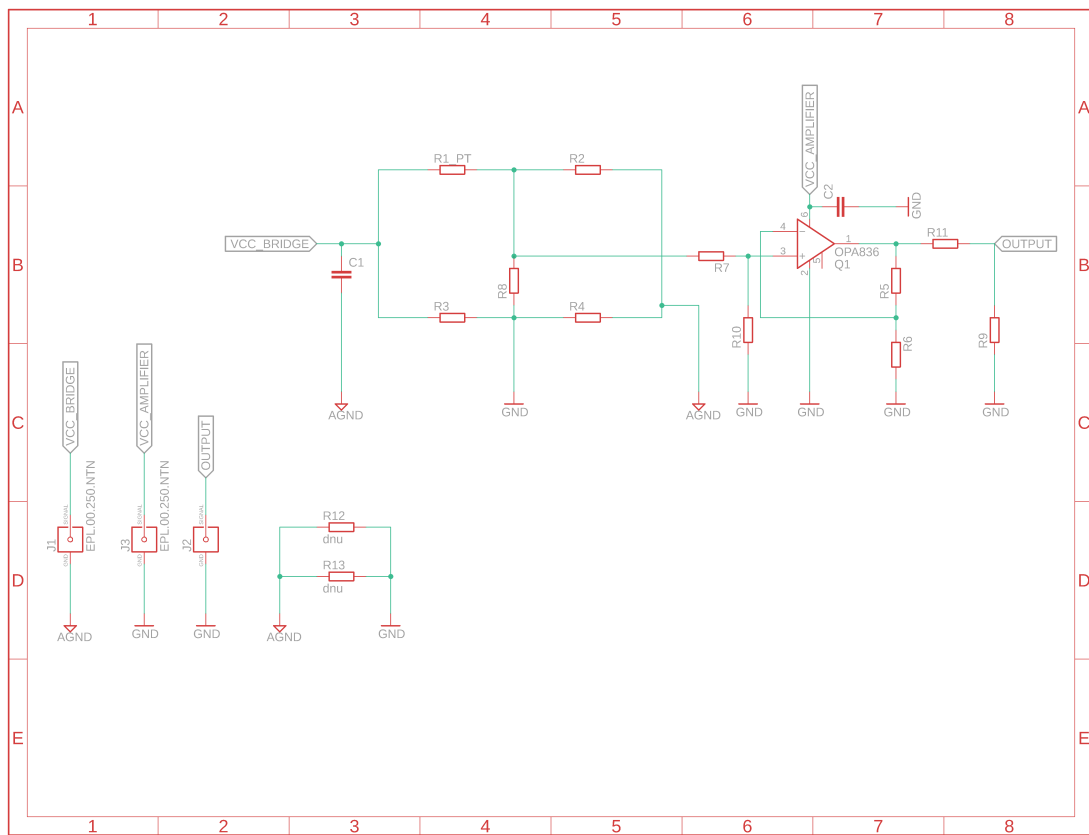


Fig. A.4: Pt100 sensor readout electronics schematic.

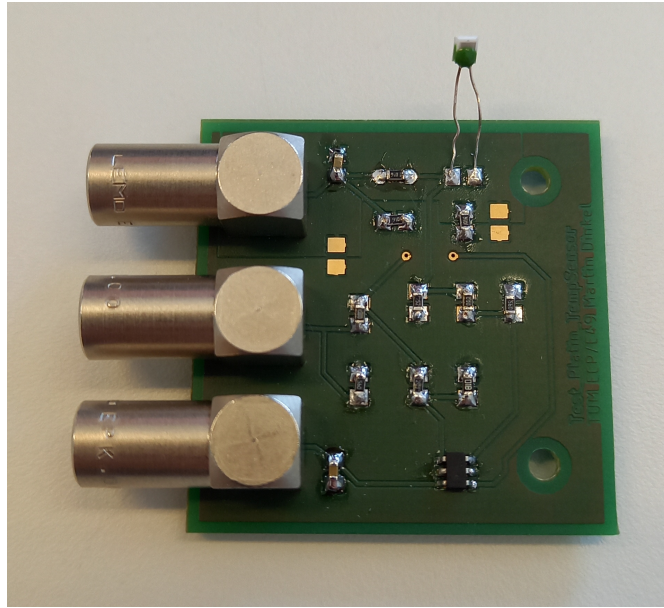


Fig. A.5: Picture of the populated board of the readout electronics of the Pt100 sensor. The used electronic components are listed in table 4.

electronic component	used values
R1_PT	91 k $\Omega$
R2	Pt100 sensor
R3	91 k $\Omega$
R4	91 k $\Omega$
R5	24 k $\Omega$
R6	1 k $\Omega$
R7	Jumper
R8	7.5 k $\Omega$
R9	56 $\Omega$
R10	56 $\Omega$
R11	Jumper
R12	dnu
R13	dnu
C1	100 nF
C2	100 nF

Tab. 4: Listing of the used values for the electronic components of the board of the Pt100 sensor.

### A.3 Temperature Chamber Programs

Preset Temperature of the TC [ $^{\circ}C$ ]	Duration of the Temperature hold [s]
-1	1800
-0,8	1800
-0,6	1800
⋮	⋮
1,6	1800
1,8	1800
2	1800
2,1	1800
2,2	1800
⋮	⋮
3,8	1800
3,9	1800
4	1800
4,2	1800
4,4	1800
4,6	1800
4,8	1800
5	1800
4,8	1800
4,6	1800
4,4	1800
4,2	1800
4	1800
3,9	1800
3,8	1800
⋮	⋮
2,1	1800
2	1800
1,8	1800
1,6	1800
⋮	⋮
-0,8	1800
-1	1800

Tab. 5: Program of the Temperature Chamber for the measurement for the general characterization of the different temperature sensors.

Preset Temperature of the TC [ $^{\circ}C$ ]	Duration of the Temperature hold [s]
-1	60
-0,8	60
-0,6	60
-0,4	60
$\vdots$	$\vdots$
1,6	60
1,8	60
2	60
2,1	60
2,2	60
2,3	60
$\vdots$	$\vdots$
3,7	60
3,8	60
3,9	60
4	60
4,2	60
4,4	60
4,6	60
4,8	60
5	60

Tab. 6: Program of the Temperature Chamber for the measurement for the detailed characterization of the different temperature sensors.

Preset Temperature of the TC [ $^{\circ}C$ ]	Duration of the Temperature hold [s]
-2	7200
20	7200
-2	7200
20	7200
-2	7200
20	7200
-2	7200
20	7200
-2	7200

Tab. 7: Program of the Temperature Chamber for the measurement of the response time of the temperature sensors.

Preset Temperature of the TC [ $^{\circ}C$ ]	Duration of the Temperature hold [s]
-2	3600
0	1800
2	1800
4	1800
3,9	300
3,8	300
3,7	300
3,6	300
3,5	300
3,2	300
3,1	300
3,0	300
⋮	⋮
2,2	300
2,1	300
2	300
1,8	300
1,6	300
1,4	300
⋮	⋮
-1,6	300
-1,8	300
-2	300

Tab. 8: Program of the Temperature Chamber for the measurement of four TMP 117 digital temperature sensors of different production lines.

Preset Temperature of the TC [ $^{\circ}C$ ]	Duration of the Temperature hold [s]
-50	3600
80	5400
-50	5400
80	5400
-50	5400
80	5400
-50	5400
80	5400
-50	5400
80	5400
-50	5400
10	1800
5	900
0	900
2	300
2,1	300
2,2	300
2,3	300
$\vdots$	$\vdots$
3,2	300
3,4	300
3,5	300
3,6	300
3,7	300
3,8	300
3,9	300
4	300

Tab. 9: Program of the Temperature Chamber for the measurement for stress test of the TMP 117 digital temperature sensor.

## A.4 Arduino Programs

Listing 1: Arduino Nano Board Program for the measurement of the general characterization of the different temperature sensors.

```
#include "TMP117.h"

uint8_t ADDR_GND = 0x48;
uint8_t ADDR_VCC = 0x49;
uint8_t ADDR_SDA = 0x4A;
uint8_t ADDR_SCL = 0x4B;
uint8_t ADDR = ADDR_GND;

int supplyPin = 8;
int value = 0;
float voltage;

TMP117 tmp(ADDR);

void setup() {
  pinMode(supplyPin, OUTPUT);
  digitalWrite(supplyPin, HIGH);
  delay(100);
  Wire.begin();
  Serial.begin(115200);
  Serial.println("Setup completed");
}

void loop() {
  value = analogRead(A0);
  voltage = value * 5.0/1023;
  Serial.print("Voltage=");
  Serial.print(voltage);
  Serial.print(" Temperature:");
  Serial.print(tmp.getTemperature());
  Serial.println(" degree Celsius");
  delay(30000);
}
```

Listing 2: Arduino Nano Board Program for the measurement of the detailed characterization of the different temperature sensors.

```
#include "TMP117.h"

uint8_t ADDR_GND = 0x48;
uint8_t ADDR_VCC = 0x49;
uint8_t ADDR_SDA = 0x4A;
uint8_t ADDR_SCL = 0x4B;
uint8_t ADDR = ADDR_GND;

int supplyPin = 8;
int value = 0;
float voltage;

TMP117 tmp(ADDR);

void setup() {
  pinMode(supplyPin, OUTPUT);
  digitalWrite(supplyPin, HIGH);
  delay(100);
  Wire.begin();
  Serial.begin(115200);
  Serial.println("Setup_completed");
}

void loop() {
  value = analogRead(A0);
  voltage = value * 5.0/1023;
  Serial.print("Voltage=");
  Serial.print(voltage);
  Serial.print(" Temperature: ");
  Serial.print(tmp.getTemperature());
  Serial.println(" degree Celsius");
  delay(5000);
}
```

Listing 3: Arduino Nano Board Program for the measurement of the response time of the temperature sensors.

```
#include "TMP117.h"

uint8_t ADDR_GND = 0x48;
uint8_t ADDR_VCC = 0x49;
uint8_t ADDR_SDA = 0x4A;
uint8_t ADDR_SCL = 0x4B;
uint8_t ADDR = ADDR_GND;

int supplyPin = 8;
int value = 0;
float voltage;

TMP117 tmp(ADDR);

void setup() {
  pinMode(supplyPin, OUTPUT);
  digitalWrite(supplyPin, HIGH);
  delay(100);
  Wire.begin();
  Serial.begin(115200);
  Serial.println("Setup_completed");
}

void loop() {
  value = analogRead(A0);
  voltage = value * 5.0/1023;
  Serial.print("Voltage=");
  Serial.print(voltage);
  Serial.print(" _Temperature_: ");
  Serial.print(tmp.getTemperature());
  Serial.println(" _degree_Celsius");
  delay(15000);
}
```

Listing 4: Arduino Nano Board Program for the measurement of four TMP 117 digital temperature sensors of different production lines.

```
#include "TMP117.h"

uint8_t ADDR_GND = 0x48; // 1001000
uint8_t ADDR_VCC = 0x49; // 1001001
uint8_t ADDR_SDA = 0x4A; // 1001010
uint8_t ADDR_SCL = 0x4B; // 1001011
uint8_t ADDR = ADDR_GND;

int supplyPin = 8;
int value = 0;
float voltage;

TMP117 tmp(ADDR);

void setup() {
  pinMode(supplyPin, OUTPUT);
  digitalWrite(supplyPin, HIGH);
  delay(100);
  Wire.begin();
  Serial.begin(115200);
  // tmp.setConvMode (CONTINUOUS);
  Serial.println("Setup completed");
}

void loop() {
  Serial.print(" Temperature: ");
  Serial.print(tmp.getTemperature());
  Serial.println(" degree Celsius");
  delay(10000);
}
```

Listing 5: **Arduino Nano Board Program for the measurement for the stress test of the TMP 117 digital temperature sensor.**

```
#include "TMP117.h"

uint8_t ADDR_GND = 0x48; // 1001000
uint8_t ADDR_VCC = 0x49; // 1001001
uint8_t ADDR_SDA = 0x4A; // 1001010
uint8_t ADDR_SCL = 0x4B; // 1001011
uint8_t ADDR = ADDR_GND;

int supplyPin = 8;
int value = 0;
float voltage;

TMP117 tmp(ADDR);

void setup() {
  pinMode(supplyPin, OUTPUT);
  digitalWrite(supplyPin, HIGH);
  delay(100);
  Wire.begin();
  Serial.begin(115200);
  // tmp.setConvMode (CONTINUOUS);
  Serial.println("Setup completed");
}

void loop() {
  Serial.print (" Temperature: ");
  Serial.print (tmp.getTemperature());
  Serial.println (" degree Celsius");
  delay(30000);
}
```

---

**List of abbreviations**

<b>AGN</b> Active Galactic Nuclei .....	4
<b>Baikal-GVD</b> Baikal Gigaton Volume Detector .....	8
<b>CC</b> charged current .....	4
<b>CMB</b> Cosmic Microwave Background .....	3
<b>DOMs</b> Digital Optical Modules .....	8
<b>GRBs</b> Gamma Ray Bursts .....	4
<b>IC</b> Integrated Circuit .....	18
<b>LiDAR</b> Light Detection and Ranging Modules .....	13
<b>LIGO</b> Laser Interferometer Gravitational-Wave Observatory .....	2
<b>NC</b> neutral current .....	4
<b>NEPTUNE</b> North East Pacific Time-series Underwater Networked Experiment .....	8
<b>OMs</b> Optical Modules .....	8
<b>ONC</b> Ocean Networks Canada .....	8
<b>PCB</b> printed circuit board .....	20
<b>PMNS</b> Pontecorvo-Maki-Nakagawaa-Sakata .....	2
<b>PMT</b> Photomultiplier Tube .....	10
<b>PMTs</b> Photomultiplier Tubes .....	7

**POCAMs** Precision Optical Calibration Modules ..... 12

**PSU** power supply unit ..... 22

**Pt100 sensor** P0K1.232.4W.K.010 Platinum Sensor with Wires..... 19

**PWN** Pulsar Wind Nebulae..... 4

**P-OM** P-ONE Optical Module..... 10

**P-ONE** Pacific Ocean Neutrino Experiment..... 1

**P-CAL** P-ONE Calibration Modules..... 11

**SCL** Serial Clock Line ..... 19

**SDA** Serial Data Line..... 19

**SNRs** Supernova Remnants ..... 4

**STRAW** Strings for Absorption length in Water ..... 12

**STRAW-b** P-ONE second pathfinder mission..... 12

**TC** Compact Ultra Low Temperature Chamber MC-712R..... 23

**TMP 117** TMP 117 digital temperature sensor ..... 18

**UHECR** Ultra High Energy Cosmic Rays..... 4

**VENUS** Victoria Experimental Network Under the Sea ..... 8

**V+** Power supply ..... 19

**WOM** Wavelength shifting Optical Module ..... 14

---

**List of Figures**

2.1	Signature topology for neutrino interaction types with matter. (a), (b) and (c) show the flavor dependent charged current interaction types, and (d) the flavor independent neutral current interaction process.[4] . . . . .	5
2.2	The schematic of Cherenkov light for a moving charged particle with velocity $u$ . [8]	7
3.1	Sketch of the planned P-ONE detector, the preliminary design consists of 7 clusters with 10 mooring lines each, wherein each mooring line comprises 20 modules. [16] . . . . .	9
3.2	Preliminary schematic of P-ONE-1 consisting of an anchor, a buoy, and the optical and calibration modules. In contrast to the sketch it is intended that each mooring line comprises 20 modules. [17] . . . . .	10
3.3	Current concept of the P-ONE optical module. It consists of two 17" glass hemispheres and a titanium head ring and embraces up to 16 PMTs arranged inside the housing together with the readout electronics of the PMTs. Figure kindly provided by Christian Spannfellner. . . . .	11
3.4	Current concept of the P-ONE calibration module hosted in the standard housing used to constantly monitor the optical properties and the geometry of the P-ONE detector. Next to the calibration hardware also PMTs will be arranged inside the housing to avoid blind spots in the detector volume. Figure kindly provided by Christian Spannfellner. . . . .	12
3.5	The STRAW mooring lines are two 150 m high mooring lines comprising together 3 POCAMs and 5 sDOMs as well as a Mini-Junction-Box and a buoy at each line. The STRAW mooring lines are designed to characterize the optical properties at Cascadia Basin. [15] . . . . .	13
3.6	The STRAW-b mooring line is roughly 450 m tall and comprises two buoys, an anchor and 10 module housings, wherein the modules are fitted with different components to characterize the physical conditions at Cascadia Basin. The STRAW-b Pathfinder has three standard modules, two PMT spectrometers, two LiDARs, one muon tracker, one mini spectrometer and one WOM. [15] . . . . .	14
4.1	Wheatstone bridge with a power supply voltage $V_{EX}$ , four resistors, wherein in each case two resistors are connected in series and the in series connected resistors are connected parallel. The voltage $V_0$ between the parallel connected circuits is measured to calculate the resistance value of one resistor when the remaining resistance values are known. [29] . . . . .	21
4.2	Experimental setup of the different temperature sensors inside the TC for the measurement for the general characterization of the different sensors. . . . .	25
4.3	Measurement data from the 40 hour measurement for the general characterization of the different temperature sensors. For more information refer to the text. . . . .	26
4.4	Measurement data from the 40 minutes measurement for the detailed characterization of the different temperature sensors. For more information refer to the text. . . . .	28

---

4.5	Section from 500 s to 2000 s of the measurement data from the 40 minutes measurement for the detailed characterization of the different temperature sensors. For more information refer to the text. . . . .	29
4.6	Pictured measurement data of the response time measurement. For more information refer to the text. For more information refer to the text. . . . .	30
4.7	Pictured measurement data of the four TMP 117 digital temperature sensors of different production batches. For more information refer to the text. . . . .	32
4.8	Measurement data of the four TMP 117 digital temperature sensors of different production batches, corrected by the offset values for $t > 2500$ s. . . . .	34
4.9	Measurement data of the four TMP 117 digital temperature sensors of different production batches, corrected by the offset values for $t > 7800$ s. . . . .	34
4.10	Cutout of the measurement data of the four TMP 117 digital temperature sensors of different production batches, corrected by the offset values for $t > 2500$ s. . . .	34
4.11	Cutout of the measurement data of the four TMP 117 digital temperature sensors of different production batches, corrected by the offset values for $t > 7800$ s. . . .	34
4.12	Experimental setup of the measurement of four TMP 117 digital temperature sensors of different production lines. The Mouser 1 sensor is located on the front right, closest to the exhaust of the TC, which is located on the right in this picture.	35
4.13	Measurement data of the stress test of the TMP 117 digital temperature sensor.	37
4.14	Measurement data of the accuracy section of the stress test of the TMP 117 digital temperature sensor. For more information refer to the text. . . . .	38
A.1	TMP 117 readout electronics schematic. . . . .	40
A.2	Front side of the populated board of the TMP 117. . . . .	41
A.3	Back side of the populated board of the TMP 117. . . . .	41
A.4	Pt100 sensor readout electronics schematic. . . . .	42
A.5	Picture of the populated board of the readout electronics of the Pt100 sensor. The used electronic components are listed in table 4. . . . .	43

---

## List of Tables

1	Selection of considered temperature sensors for the usage as a long-term temperature monitoring device in the P-ONE detector, wherein the requirements of this section 4.1 which are not fulfilled by the sensors are listed in the right column. . . . .	17
2	Results of the offset calculation for the considered time intervals. . . . .	33
3	Listing of the used values for the electronic components of the board of the TMP 117 digital temperature sensor. . . . .	41
4	Listing of the used values for the electronic components of the board of the Pt100 sensor. . . . .	43
5	Program of the Temperature Chamber for the measurement for the general characterization of the different temperature sensors. . . . .	44
6	Program of the Temperature Chamber for the measurement for the detailed characterization of the different temperature sensors. . . . .	45
7	Program of the Temperature Chamber for the measurement of the response time of the temperature sensors. . . . .	45
8	Program of the Temperature Chamber for the measurement of four TMP 117 digital temperature sensors of different production lines. . . . .	46
9	Program of the Temperature Chamber for the measurement for stress test of the TMP 117 digital temperature sensor. . . . .	47

---

## References

- [1] Imma Rea. “The Pacific Ocean Neutrino Experiment: feasibility study for a new Neutrino Telescope at Cascadia Basin, NE Pacific Ocean”. PhD thesis. 2021.
- [2] Marica Branchesi. “Multi-messenger astronomy: gravitational waves, neutrinos, photons, and cosmic rays”. In: *Journal of Physics: Conference Series* (2016), p. 022004. ISSN: 1742-6588. DOI: 10.1088/1742-6596/718/2/022004.
- [3] Christian Spannfellner. *Development of pathfinder missions and instruments for the Pacific Ocean Neutrino Experiment*. 2020.
- [4] Maurizio Spurio. *Particles and Astrophysics*. Cham: Springer International Publishing, 2015. ISBN: 978-3-319-08050-5. DOI: 10.1007/978-3-319-08051-2.
- [5] Thomas K. Gaisser, Elisa Resconi, and Ralph Engel. *Cosmic rays and particle physics*. Second edition. Cambridge: Cambridge University Press, 2016. ISBN: 9781139192194. DOI: 10.1017/CBO9781139192194.
- [6] M. Aker et al. “Direct neutrino-mass measurement with sub-electronvolt sensitivity”. In: *Nature Physics* 18.2 (2022), pp. 160–166. ISSN: 1745-2473. DOI: 10.1038/s41567-021-01463-1.
- [7] Tonia M. Venters et al. *Energetic Particles of Cosmic Accelerators II: Active Galactic Nuclei and Gamma-ray Bursts*. 2020. URL: <http://arxiv.org/pdf/1903.04639v1>.
- [8] *Schematic cherenkov light cone*. URL: <http://large.stanford.edu/courses/2014/ph241/alaecian2/>.
- [9] IceCube Collaboration et al. “Energy Reconstruction Methods in the IceCube Neutrino Telescope”. In: *Journal of Instrumentation* 9.03 (2014), P03009–P03009. DOI: 10.1088/1748-0221/9/03/P03009. URL: <http://arxiv.org/pdf/1311.4767v3>.
- [10] Simone Biagi. *Updated limits on diffuse fluxes of cosmic neutrinos with 2008-2011 ANTARES data*. 2013. URL: <http://arxiv.org/pdf/1305.6442v1>.
- [11] *IceCube Neutrino Observatory Website*. URL: <https://icecube.wisc.edu/>.
- [12] Pierluigi Traverso and KMCubeNeT Collaboration. “KM3NeT: Technical Design Report for a Deep-Sea Research Infrastructure in the Mediterranean Sea Incorporating a Very Large Volume Neutrino Telescope”. In: (July 2009).
- [13] *KM3Net Website*. URL: <https://www.km3net.org/>.
- [14] *Baikal GVD Website*. URL: <https://baikalgvd.jinr.ru/>.
- [15] Elisa Resconi. “The Pacific Ocean Neutrino Experiment”. In: *Proceedings of 37th International Cosmic Ray Conference — PoS(ICRC2021)*. Ed. by Bianca Keilhauer. Trieste, Italy: Sissa Medialab, 2021, p. 024. DOI: 10.22323/1.395.0024.
- [16] *P-ONE Website*. URL: <https://www.pacific-neutrino.org/p-one/how-p-one-will-be-designed>.
- [17] C. Spannfellner. “ICRC 2021 Prototype Line Concept”. In: (2021).

- 
- [18] M. Boehmer et al. “STRAW (STRings for Absorption length in Water): pathfinder for a neutrino telescope in the deep Pacific Ocean”. In: *Journal of Instrumentation* 14.02 (2019), P02013–P02013. DOI: 10.1088/1748-0221/14/02/P02013.
- [19] Nicolai Bailly et al. “Two-year optical site characterization for the Pacific Ocean Neutrino Experiment (P-ONE) in the Cascadia Basin”. In: *The European Physical Journal C* 81.12 (2021), p. 1071. ISSN: 1434-6052. DOI: 10.1140/epjc/s10052-021-09872-5.
- [20] *Introduction to Cascadia Basin*. URL: <https://www.oceannetworks.ca/introduction-cascadia-basin>.
- [21] Uchida et al. “Deep Ocean Temperature Measurement with an Uncertainty of 0.7mK”. In: *Journal of Atmospheric and Oceanic Technology* (2015), pp. 2199–2210.
- [22] Gregory C. Johnson, Kristene E. McTaggart, and Rik Wanninkhof. “Antarctic Bottom Water temperature changes in the western South Atlantic from 1989 to 2014”. In: *Journal of Geophysical Research: Oceans* 119.12 (2014), pp. 8567–8577. ISSN: 21699275. DOI: 10.1002/2014JC010367.
- [23] Damien G. Desbruyères et al. “Deep and abyssal ocean warming from 35 years of repeat hydrography”. In: *Geophysical Research Letters* 43.19 (2016), pp. 10, 356–10, 365. ISSN: 0094-8276. DOI: 10.1002/2016GL070413.
- [24] Elizabeth F. Gugliotti, Marie E. DeLorenzo, and Peter J. Etnoyer. “Depth-dependent temperature variability in the Southern California bight with implications for the cold-water gorgonian octocoral *Adelogorgia phyllosclera*”. In: *Journal of Experimental Marine Biology and Ecology* 514-515 (2019), pp. 118–126. ISSN: 00220981. DOI: 10.1016/j.jembe.2019.03.010.
- [25] Robert W. Schlegel and Albertus J. Smit. “Climate Change in Coastal Waters: Time Series Properties Affecting Trend Estimation”. In: *Journal of Climate* 29.24 (2016), pp. 9113–9124. ISSN: 0894-8755. DOI: 10.1175/JCLI-D-16-0014.1.
- [26] Star Oddi Ltd. *Starmon Mini datasheet*. URL: <https://www.star-oddi.com/media/1/starmon-minipl.pdf>.
- [27] *TMP117 datasheet*. URL: <https://www.ti.com/lit/ds/symlink/tmp117.pdf>.
- [28] *Pt100 application note*. URL: <https://www.ist-ag.com/sites/default/files/downloads/p0k1.232.4w.k.010.pdf>.
- [29] *Wheatstone Bridge Figure*. URL: <https://www.bestech.com.au/blogs/understanding-a-wheatstone-bridge-strain-gauge-circuit/>.
- [30] *Wheatstone Bridge*. URL: <https://www.electronics-tutorials.ws/blog/wheatstone-bridge.html>.
- [31] *Non-inverted Amplifier*. URL: <https://www.elektronik-kompodium.de/sites/slt/0210151.htm>.
- [32] *TMP117 arduino library*. URL: <https://github.com/NilsMinor/TMP117-Arduino>.